A Tale of Two Vortex Evolutions: Using a High-Resolution Ensemble to Assess the Impacts of Ventilation on a Tropical Cyclone Rapid Intensification Event

MICHAEL S. FISCHER,[a,b] PAUL D. REASOR,[b] BRIAN H. TANG,[c] KRISTEN L. CORBOSIERO,[c] RYAN D. TORN,[c] AND XIAOMIN CHEN[b,d]

[a] *Cooperative Institute for Marine and Atmospheric Studies, University of Miami, Miami, Florida*
[b] *NOAA/OAR/Atlantic Oceanographic and Meteorological Laboratory, Miami, Florida*
[c] *Department of Atmospheric and Environmental Sciences, University at Albany, State University of New York, Albany, New York*
[d] *Northern Gulf Institute, Mississippi State University, Stennis Space Center, Mississippi*

(Manuscript received 8 February 2022, in final form 23 August 2022)

ABSTRACT: The multiscale nature of tropical cyclone (TC) intensity change under moderate vertical wind shear was explored through an ensemble of high-resolution simulations of Hurricane Gonzalo (2014). Ensemble intensity forecasts were characterized by large short-term (36-h) uncertainty, with a forecast intensity spread of over 20 m s^{-1}, due to differences in the timing of rapid intensification (RI) onset. Two subsets of ensemble members were examined, referred to as early-RI and late-RI members. The two ensemble groups displayed significantly different vortex evolutions under the influence of a nearby upper-tropospheric trough and an associated dry-air intrusion. Mid-to-upper-tropospheric ventilation in late-RI members was linked to a disruption of inner-core diabatic heating, a more tilted vortex, and vortex breakdown, as the simulated TCs transitioned from a vorticity annulus toward a monopole structure. A column-integrated moist static energy (MSE) budget revealed the important role of horizontal advection in depleting MSE from the TC core, while mesoscale subsidence beneath the dry-air intrusion acted to dry a deep layer of the troposphere. Eventually, the dry-air intrusion retreated from late-RI members as vertical wind shear weakened, the magnitude of vortex tilt decreased, and late-RI members began to rapidly intensify, ultimately reaching a similar intensity as early-RI members. Conversely, the vortex structures of early-RI members were shown to exhibit greater intrinsic resilience to tilting from vertical wind shear, and early-RI members were able to fend off the dry-air intrusion relatively unscathed. The different TC intensity evolutions can be traced back to differences in the initial TC vortex structure and intensity.

SIGNIFICANCE STATEMENT: Despite recent advances, tropical cyclone intensity forecasts struggle to accurately predict episodes of rapid intensification. Such forecasts become increasingly challenging when a storm is embedded within an environment of moderate vertical wind shear. This study uses an ensemble of high-resolution simulations to examine how environmental influences can affect the tropical cyclone vortex and precipitation structure, which, in turn, modulate the intensity of the storm and the onset of rapid intensification. We propose a feedback that exists where slightly weaker and less resilient vortices are more susceptible to ventilation from dry, environmental air, aided in part by differential advection from the tilted circulation, resulting in a degradation of vortex organization and a delayed onset of rapid intensification.

KEYWORDS: Convection; Wind shear; Tropical cyclones; Ensembles; Numerical analysis/modeling

1. Introduction

Predicting tropical cyclone (TC) intensity change in environments of moderate vertical wind shear is particularly challenging (Bhatia and Nolan 2013). Empirically, it has been well documented that environments with larger magnitudes of vertical wind shear tend to be unfavorable for TC intensification (DeMaria and Kaplan 1994; Kaplan et al. 2015; Rios-Berrios and Torn 2017); however, TCs in environments of moderate vertical wind shear (e.g., a deep-layer shear magnitude of approximately 5–10 m s^{-1}) are associated with a wide range of TC intensity changes, including both weakening episodes as well as TC rapid intensification (RI; Nguyen and Molinari 2012; Rogers et al. 2015; Rios-Berrios and Torn 2017; Chen et al. 2018b; Hazelton et al. 2020). Although accurately predicting RI remains a tremendous endeavor regardless of the environmental regime (Gall et al. 2013; Kaplan et al. 2015; Cangialosi et al. 2020), TCs in environments of moderate shear are especially problematic, as such events tend to be associated with greater uncertainty in the timing of RI onset (Zhang and Tao 2013; Tao and Zhang 2015, 2019). Considering the vast societal impacts imposed by TCs that undergo RI prior to landfall, it is imperative we acquire an improved understanding of the factors that dictate the rate of TC intensity change, as well as the timing of RI onset, in environments of moderate vertical wind shear.

This challenge remains despite a substantial body of existing literature that has documented multiple pathways through which environmental vertical wind shear can affect the TC vortex. One primary consequence of vertical wind shear is differential advection of the TC potential vorticity (PV) column, which initially tilts the vortex downshear (Jones 1995;

Corresponding author: Michael S. Fischer, michael.fischer@noaa.gov

DOI: 10.1175/MWR-D-22-0037.1

Reasor et al. 2004). In accordance with thermal wind balance, a tilted column of PV is associated with local temperature perturbations (Jones 1995; DeMaria 1996). As air cyclonically orbits the vortex, the balanced response yields ascent in regions of upward slanted isentropes and, thus, the tilt direction has a strong influence on the TC precipitation structure (e.g., Ryglicki et al. 2018; Boehm and Bell 2021). The direction of vortex tilt is dynamic, however, and the upper portion of a tilted TC vortex can oscillate (Ryglicki et al. 2018, 2021) or precess (Rappin and Nolan 2012; Reasor and Montgomery 2015; Rios-Berrios et al. 2018) around its lower-tropospheric counterpart. Idealized simulations and observations agree that the vortex tilt orientation is most stable when the tilt is directed along, and to the left of, the vertical wind shear vector (Jones 1995; Reasor et al. 2004, 2013; Reasor and Montgomery 2015). Consistent with these results, composite analyses have found a clear preference for downshear convection (Corbosiero and Molinari 2002; Reasor et al. 2013; DeHart et al. 2014; Fischer et al. 2018) and enhanced boundary layer inflow (Reasor et al. 2013; DeHart et al. 2014). As the magnitude of vertical shear increases, convective asymmetries become increasingly pronounced (Chen et al. 2006), which is typically an unfavorable configuration for large rates of TC intensification (Nolan and Grasso 2003; Alvey et al. 2015; Fischer et al. 2018).

Nevertheless, some TCs display resiliency in the midst of vertically sheared environmental flow and achieve a sustained period of vortex alignment. Both numerical simulations (Tao and Zhang 2014; Rios-Berrios et al. 2018; Chen et al. 2019; Alvey et al. 2020; Hazelton et al. 2020) and observational studies (Stevenson et al. 2014; Rogers et al. 2015; Susca-Lopata et al. 2015; Rogers et al. 2020) have demonstrated that vortex alignment often precedes RI, as vortex alignment promotes more symmetric precipitation (Tao and Zhang 2014; Munsell et al. 2017; Chen et al. 2018b; Alvey et al. 2020). Thus, TC intensity change in the presence of shear is closely related to the resiliency of the TC vortex.

Multiple hypotheses have been put forth to describe the nature of TC resiliency and vortex alignment. One possible pathway toward alignment involves the vertical coupling of the TC vortex, which induces a cyclonic precession of the mid-to-upper-level vortex about the low-level vortex center (Jones 1995). If the mid-to-upper-level vortex precesses into the upshear quadrants, alignment can be achieved via the differential advection of the upper-level vortex center toward the low-level center by the sheared environmental flow. Other views of vortex resiliency involve the generation of vortex Rossby waves (VRWs) by the sheared environmental flow (Schecter et al. 2002; Reasor et al. 2004; Reasor and Montgomery 2015). Using dry dynamics, Reasor et al. (2004) demonstrated an intrinsic tilt reduction mechanism governed by the damping of a vortex tilt mode in the midst of shear. Diabatic heating associated with the TC overturning circulation was believed to contribute indirectly to the resiliency of the vortex by increasing the efficiency of the VRW damping mechanism via a reduction of static stability in regions of moist ascent (Reasor et al. 2004; Schecter and Montgomery 2007; Reasor and Montgomery 2015; Schecter 2015). For storms below hurricane intensity, other studies have argued diabatic processes are essential for the alignment of a tilted TC vortex (Schecter and Menelaou 2020), whether alignment occurs through either a vortex merger process (Rios-Berrios et al. 2018) or by downshear center reformations within the broader TC parent vortex (Nguyen and Molinari 2015; Chen et al. 2018a; Rogers et al. 2020; Alvey et al. 2022).

In addition to tilting the TC vortex, vertical wind shear can also ventilate the TC warm core with low-entropy environmental air, effectively limiting the efficiency of the TC heat engine (Simpson and Riehl 1958; Emanuel et al. 2004). The ventilation of the TC warm core has been hypothesized to occur through multiple routes. In one such pathway, vertical wind shear induces eddy fluxes that transport high-equivalent potential temperature and high-potential vorticity radially outward in the upper troposphere, which act to weaken the TC from the top down (Frank and Ritchie 2001; Kwon and Frank 2008). Alternatively, vertical wind shear can excite azimuthal asymmetries that flux low-entropy, midtropospheric environmental air radially inward toward the TC inner core (Cram et al. 2007; Tang and Emanuel 2010, 2012; Alland et al. 2021b). Midtropospheric ventilation acts to weaken the storm by reducing the mechanical efficiency of the TC heat engine and reducing the radial gradient of equivalent potential temperature associated with the eyewall front (Tang and Emanuel 2012). In some cases, persistent downshear precipitation asymmetries can flux low-entropy air downward into the boundary layer before entering the TC eyewall (Riemer et al. 2010, 2013; Alland et al. 2021a). This low-level ventilation pathway can be more capable of frustrating the TC heat engine than ventilation occurring at higher levels in the troposphere (Riemer et al. 2010; Tang and Emanuel 2012); however, surface fluxes can act to replenish low-entropy downdraft air before it reaches the TC inner core (e.g., Tang and Emanuel 2012; Chen et al. 2021; Wadler et al. 2021).

Recently, these ventilation pathways have been concisely recategorized as either downdraft ventilation (Alland et al. 2021a) or radial ventilation (Alland et al. 2021b) depending on the predominant direction of the transport of low-entropy air. Through the utilization of a bivariate parameter space, Alland et al. (2021a,b) examined sets of idealized simulations to assess how both downdraft and radial ventilation affect TC structure and intensity change by varying environmental shear and humidity. Downdraft ventilation was associated with the downward transport of negatively buoyant air, primarily occurring immediately cyclonically downstream of the vortex tilt direction (Alland et al. 2021a). The intensity of downdraft ventilation increased for more tilted vortices. Radial ventilation was also found to be closely connected to TC vortex tilt, as the cyclonic flow associated with the tilted midlevel vortex imported dry air into the upshear and right-of-shear regions of the TC (Alland et al. 2021b). Together, the two ventilation pathways act to reduce the areal extent of moist convection, thereby impeding TC development. These results illustrate the important link between vertical wind shear, vortex tilt, ventilation, and TC intensity change.

The present study aims to explore how radial and downdraft ventilation affect TC intensity change in nonidealized vortices using a high-resolution ensemble framework. Specifically, we

TABLE 1. List of physical parameterizations used in the AHW ensemble simulations.

Parameterization	Reference
Modified Tiedtke cumulus convection	Zhang et al. (2011)
Rapid radiative transfer longwave and shortwave radiation	Mlawer et al. (1997)
WRF single-moment 6-class (WSM6) microphysics	Hong et al. (2004)
Yonsei University (YSU) planetary boundary layer	Hong et al. (2006)

will investigate simulations of Hurricane Gonzalo (2014) during a period when there was large uncertainty in the forecast intensity as the TC interacted with an upper-tropospheric trough and an associated dry-air intrusion in an environment of moderate vertical wind shear. We will show that TC intensity change and the timing of RI onset is closely related to the initial TC intensity and degree of vortex misalignment, the resilience of the TC vortex, and the impacts of ventilation on the TC thermodynamic state and convective structure.

2. Modeling setup

Ensemble forecasts of Hurricane Gonzalo were generated using the Advanced Hurricane Weather Research and Forecasting (WRF) Model (AHW; Davis et al. 2008a). AHW forecasts were produced in real-time from 2009 to 2014 as part of the Hurricane Forecast Improvement Project (HFIP; Gall et al. 2013) and have been utilized by multiple previous studies to assess a range of TC processes (e.g., Davis et al. 2010; Torn and Davis 2012; Torn and Cook 2013; Rios-Berrios et al. 2016a,b; Torn 2016). The data assimilation procedures utilized here closely follow those documented in Cavallo et al. (2013). Of interest to this study, a suite of 60 ensemble member forecasts were run using initial conditions taken from a cycling ensemble Kalman filter (EnKF) data assimilation system. The only differences between ensemble members are coherent perturbations, on the order of analysis errors (Cavallo et al. 2013), to both the initial and boundary conditions.

The present modeling setup involves multiple nested domains with 36-, 12-, 4-, and 1.33-km grid spacing. The outermost domain (36 km) is static, spanning the width of the Atlantic basin, while the remaining three domains follow the TC location, with domain sizes of approximately 1600 km × 1600 km, 1200 km × 1200 km, and 600 km × 600 km, for the 12-, 4-, and 1.33-km nests, respectively. The model parameterizations used herein are listed in Table 1. It should be noted that the 4- and 1.33-km nests do not have a cumulus parameterization. Ensemble simulations were initialized at 1200 UTC 13 October 2014—near the start of an observed RI event—and ran for a 72-h period, with output saved hourly. For select ensemble members, output was stored at 6-min intervals.

3. Characteristics of the ensemble forecasts

Figure 1 shows forecast intensity traces, beginning at the model initialization. The observed intensity of Hurricane Gonzalo fell within the spread of ensemble forecasts of both minimum sea level pressure (Fig. 1a) and maximum sustained 10-m wind speed (Fig. 1b) throughout the majority of the forecast period. The ensemble features a significant spread in intensity 24–48 h into the simulations, with the difference between the most intense and weakest members approaching 30 m s^{-1} by forecast hour 30.

To investigate potential causes of the large forecast intensity spread, two groups of ensemble members were identified. These groups correspond to the top and bottom 15th percentiles of the 0–48-h time-averaged minimum sea level pressure. The intensity evolutions of the nine members in each group are shown by the red and blue lines in Fig. 1.

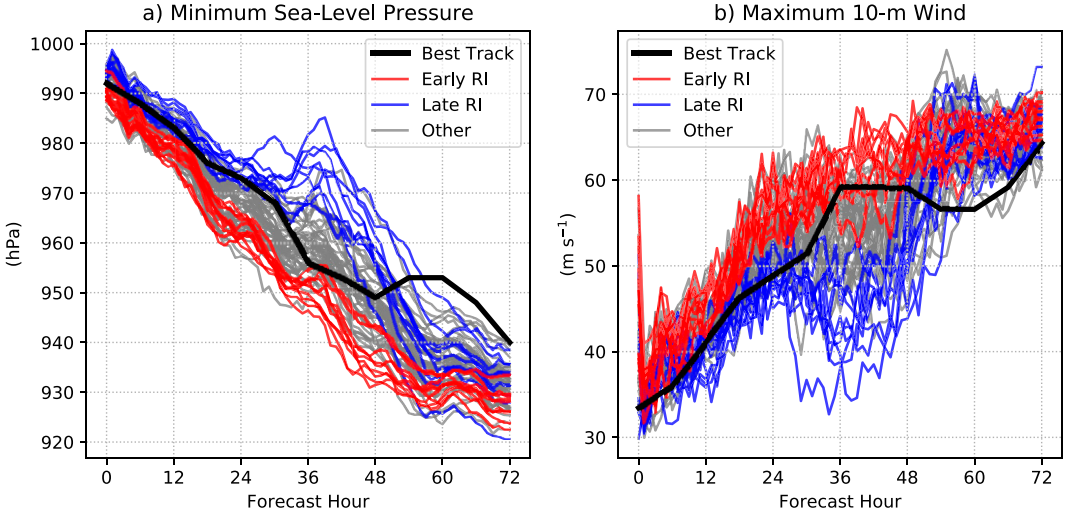

FIG. 1. (a) Ensemble forecasts of minimum sea level pressure (hPa) for early-RI members (red), late-RI members (blue), and other members (gray). Forecasts are initialized at 1200 UTC 13 Oct 2014. The best track intensity for the corresponding times is shown by the black line. (b) As in (a), but for maximum sustained 10-m wind speed (m s^{-1}).

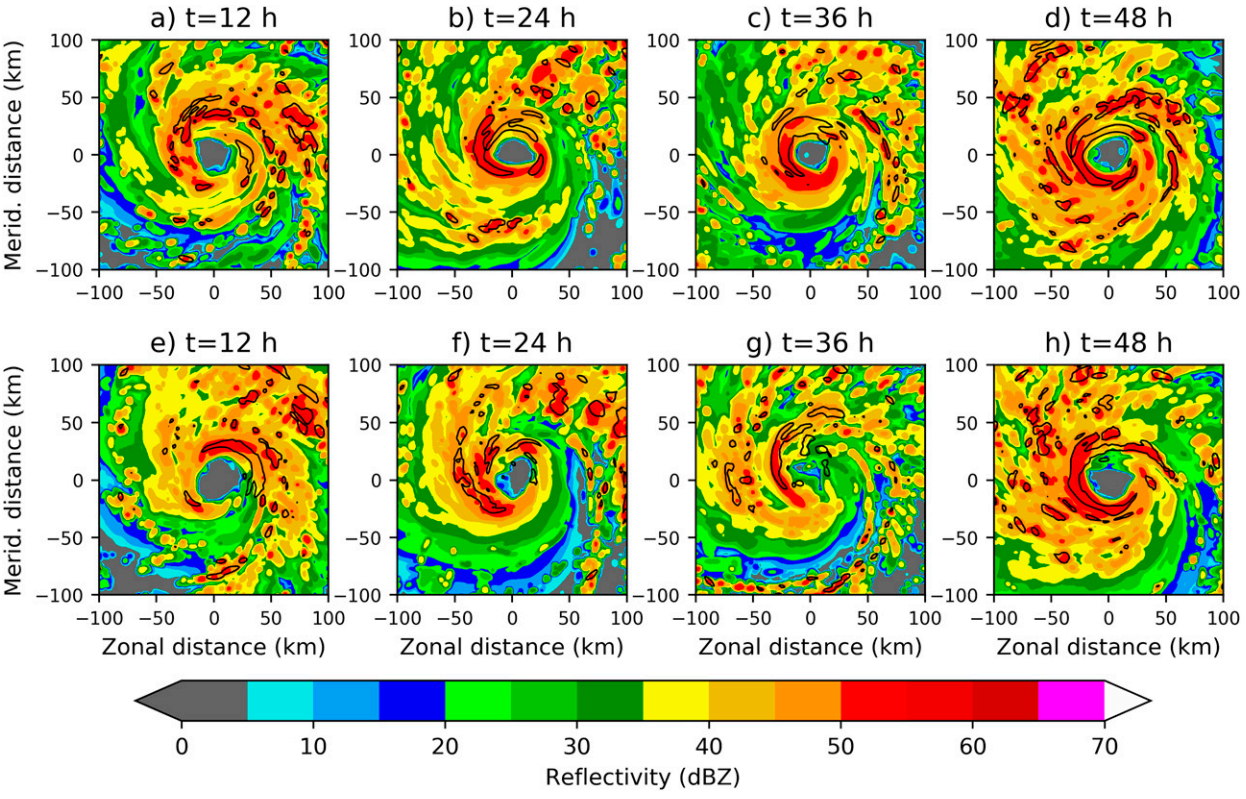

FIG. 2. Storm-centered, column-maximum simulated radar reflectivity (shaded; dBZ) for a representative (top) early-RI member and (bottom) late-RI member. Snapshots are shown at (a),(e) 12; (b),(f) 24; (c),(g) 36; and (d),(h) 48 h into the simulations. Layer-mean, 700–400-hPa vertical velocity ($V_\omega = dp/dt$) < -10 Pa s^{-1} is shown in the black contours.

Each ensemble group is characterized by a distinct intensity evolution. The first group—comprising the strongest ensemble members through the first 48 h—is associated with a period of RI through the first 36 h of the simulations, followed by a period of more gradual intensification. Hence, this group of ensemble members is hereafter referred to as the "early-RI" group. Alternatively, the second group of ensemble members—comprising the weakest members through the first 48 h—are associated with an initial period of slower intensification, followed by a period of slight weakening between approximately 24 and 42 h, before ultimately undergoing RI around 48 h into the simulations. As a result, this group of ensemble members is hereafter referred to as the "late-RI" group.

Storm-centered[1] snapshots of the structural evolution of a representative early-RI and late-RI member are shown in Fig. 2. Within the first 24 h of the forecast period, a well-defined eye is present in both the early-RI and late-RI members, although the early-RI member has a greater coverage of reflectivities ≥ 30 dBZ in the southern sector of the storm (Figs. 2a,b,e,f). At 36 h into the simulations, the early-RI member maintains a well-defined eyewall (Fig. 2c); however, the inner-core organization of the late-RI member has dramatically deteriorated (Fig. 2g). This degradation of the late-RI member's inner core is consistent with the slight weakening most late-RI members experience near this time (Fig. 1). By 48 h into the simulations, both the early- and late-RI members display improved organization, with a more symmetric region of robust ascent associated with the TC eyewall (Figs. 2d,h). The late-RI member's sharp increase in organization at 48 h (Fig. 2h) agrees with the more rapid rates of intensification at this time (Fig. 1). Although not shown here, early-RI and late-RI members were associated with similar track forecasts, which suggest their large intensity differences are due to processes beyond those arising from differing tracks.

4. Environmental influences on the rate of TC intensification

a. *Environmental overview*

Figure 3a shows the distribution of the deep-layer vertical wind shear magnitude for early- and late-RI members. Here, the vertical wind shear is calculated as the vector difference of the area-averaged wind between 850 and 200 hPa within

[1] The TC center was defined using a method similar to Nguyen et al. (2014), where the TC center was determined using an iterative process that identified the sea level pressure centroid. Here, all values within a 100 km × 100 km box, initially centered on the minimum sea level pressure location, were used in the computation.

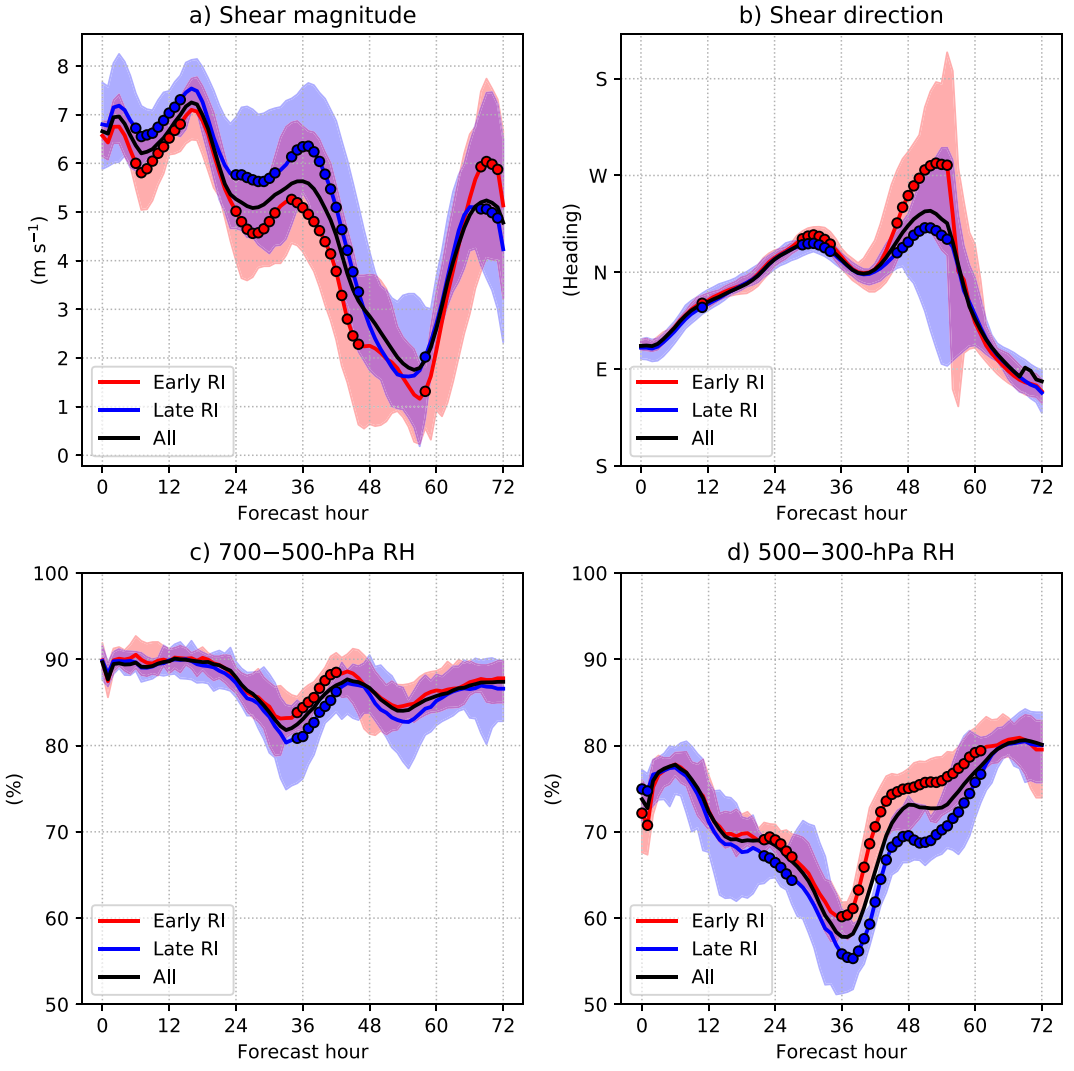

FIG. 3. (a) Composite-mean ensemble forecasts of 850–200-hPa vertical wind shear magnitude (m s^{-1}) for early-RI members (red), late-RI members (blue), and all members (black). Red-shaded regions span the entire distribution of early-RI members, while blue-shaded regions span the distribution of late-RI members. Dotted points denote times where the differences between early and late-RI members are statistically significant at the 95% confidence level. (b)–(d) As in (a), but for the 850–200-hPa vertical wind shear direction (heading of shear vector shown), 700–500-hPa layer-averaged relative humidity (%), and the 500–300-hPa layer-averaged relative humidity, respectively.

a 0–500-km storm-centered disc. For most of the forecast period, the simulated TCs are embedded in environments of moderate vertical wind shear magnitudes between 4 and 8 m s^{-1}, with the exception of a period between approximately 42 and 60 h into the simulations, where the shear drops to roughly 2 m s^{-1}. Although both early- and late-RI members exhibit a similar shear evolution, early-RI members are generally associated with shear magnitudes 0.5–1 m s^{-1} less than those of late-RI members. The period of largest differences is found about 24–48 h into the forecast period, coinciding with the time of the largest forecast intensity differences (Fig. 1). The differences in shear between early- and late-RI members were determined to be statistically significant[2] for the majority of the first 42 h of the forecast period. Unlike the deep-layer vertical wind shear magnitude, the vertical wind shear direction for early- and late-RI ensemble members were largely similar over the forecast period, with the exception of the period between approximately 48 and 54 h into the forecast period (Fig. 3b) when the shear magnitude was rapidly decreasing (Fig. 3a).

[2] The statistical significance tests performed in the present study use the non-parametric, two-tailed Wilcoxon rank sum test. Distributions were determined to be statistically significantly different if they met or exceeded the 95% confidence level (p value ≤ 0.05).

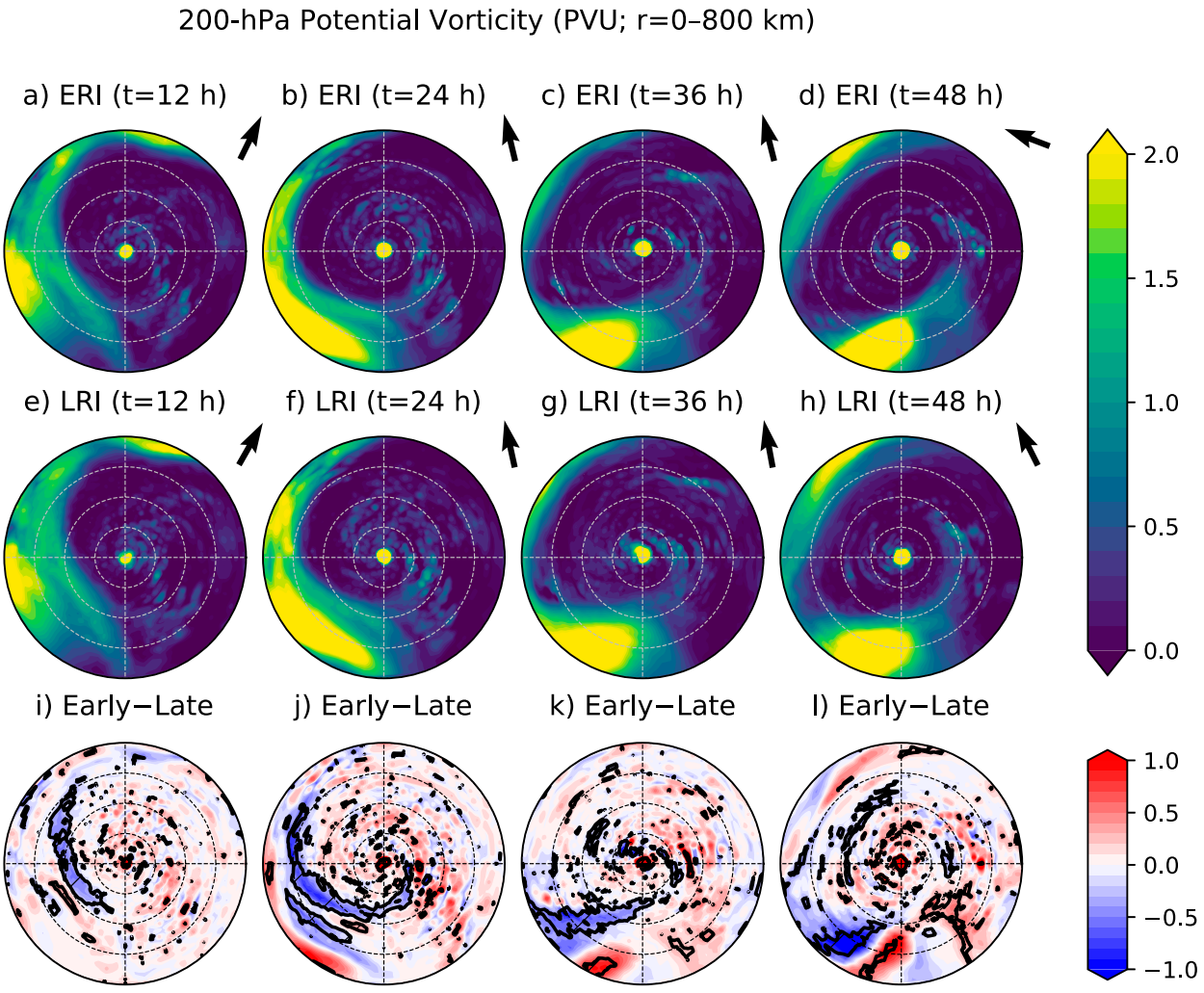

FIG. 4. Storm-centered, 0–800-km, composite-mean potential vorticity (shaded; PVU) on the 200-hPa isobaric surface for early-RI members. Forecasts are valid at (a) 12, (b) 24, (c) 36, and (d) 48 h. Here, dashed radial rings are spaced in 200-km increments. The 850–200-hPa shear direction is shown by the black vectors. (e)–(h) As in (a)–(d), but for late-RI members. (i)–(l) As in (a)–(d), but for the composite-mean PV difference of early-RI members minus late-RI members. Regions that are statistically significantly different at the 95% confidence level are shown by the black contours and hatching.

Figures 3c and 3d show the evolution of near-storm (0–200-km) relative humidity for both early- and late-RI members averaged between 700–500 and 500–300 hPa, respectively. Humidity differences between the two ensemble groups are more pronounced in the 500–300-hPa layer (Fig. 3d). In both the 700–500-hPa and 500–300-hPa layers, the minimum domain-averaged relative humidity is found near forecast hour 36, with early-RI members associated with significantly more moist near-core environments than late-RI members, coinciding with the time with the largest TC intensity (Fig. 1) and structural differences (Figs. 2c,g). Although it is possible differences in vortex structure and intensity between early- and late-RI members are contributing to the different near-core relative humidity evolutions, these results suggest late-RI members may have suffered from greater ventilation of the TC inner core with dry, environmental air, and motivates a deeper investigation into the simulated TC environment.

b. *Interaction with an upper-tropospheric trough*

The synoptic environment of Hurricane Gonzalo was influenced by an upper-tropospheric trough, initially located to the west of the TC. Figure 4 shows the evolution of the trough via composite maps of 200-hPa PV for early- and late-RI members, in 12-h increments. Here, the trough is reflected by the region of relatively large PV [e.g., 200-hPa PV $\geq$ 1 PVU (1 PVU = 10^{-6} K kg^{-1} m^2 s^{-1})] initially located to the west of the TC. In both ensemble groups, the cyclonic flow associated with the upper-tropospheric trough heavily influenced both the magnitude, and direction, of the vertical wind shear. As the trough moved cyclonically, from the western to southern side of Gonzalo during the first 36 h of the forecast period

(Figs. 4a–c,e–g), the vertical wind shear direction also shifted cyclonically, from an eastward heading toward a northward heading (Fig. 3b).

Despite the qualitatively similar upper-tropospheric trough evolutions in early- and late-RI members, some slight, but statistically significant differences in the position of the trough were identified. During the first 12–36 h, early-RI members were associated with an upper-tropospheric trough with a statistically significant greater distance from the TC center than late-RI members (Figs. 4i–k). Previous observational work has shown a larger upstream distance between the TC and trough is favorable for RI, as such configurations tend to be associated with weaker environmental vertical wind shear (Fischer et al. 2019). Consistent with these observational findings, the greater upstream trough displacement in early-RI members is linked to weaker vertical wind shear magnitudes than late-RI members (Fig. 3a). By 48 h into the forecast period, the upper-tropospheric trough position differences now peak within the same radial band, approximately 600 km away from the TC location (Fig. 4l), indicating the troughs in early-RI members are no longer farther away from the TC than late-RI members. Instead, the trough location differences resemble an azimuthal position shift. It is at this time the differences in vertical wind shear magnitude between early- and late-RI members lessen (Fig. 3a).

c. *Influences of a midlevel dry-air intrusion*

In addition to the connection between the upper-tropospheric trough position and vertical wind shear, previous work has shown upper-tropospheric troughs can be associated with unfavorable dry-air intrusions (Leroux et al. 2013; Zhang et al. 2016). Time series of azimuthally averaged, relative humidity indicate a dry-air intrusion may have occurred between forecast hours 24 and 48 (Figs. 3c,d). To examine the structure and evolution of this potential dry-air intrusion, Fig. 5 displays storm-centered, composite-mean, 400-hPa relative humidity for early- and late-RI members. Here, storm-relative inflow is overlaid in dashed contours to identify regions where dry air was advected toward the TC core. Although the dry-air intrusion encompassed much of the mid- to upper troposphere, the 400-hPa level reveals prominent differences between the two ensemble groups.

By 12 h into the simulations, early- and late-RI members are associated with asymmetric moisture fields, as the regions of the greatest relative humidity are primarily located downshear of the TC center (Figs. 5a,e). Although both groups display a region of relative humidity $< 50\%$ to the left of the shear direction, early-RI TCs are associated with greater areal coverage of near-saturated air, with significant differences extending into the upshear-left quadrant within 100 km of the TC center (Fig. 5i). The greater humidity in the upshear-left quadrant of early-RI TCs corroborates other studies that have emphasized the importance of moistening in this region for TC intensification (Rios-Berrios and Torn 2017; Rios-Berrios et al. 2018; Alvey et al. 2020; Hazelton et al. 2020; Alland et al. 2021a,b).

The vertical wind shear vector, the inflow region, and the dry-air intrusion rotate cyclonically by forecast hour 24 (Figs. 5b,f). The dry-air intrusion is now more pronounced, with minimum 400-hPa relative humidity $< 25\%$ within 200 km of the TC. Differences between early- and late-RI members have also grown in area, as late-RI members are associated with a region of statistically significant drier air that nearly encircles the TC center immediately outside of the eyewall region, approximately 30–50 km from the TC center (Fig. 5j). This region of significantly drier air extends outward to nearly 200 km in the upshear quadrants, indicative of a lesser upshear extent of the moist, precipitation shield in late-RI members (Fig. 5j).

By forecast hour 36, the relative humidity field has grown highly asymmetric as the dry-air intrusion has advanced closer toward the TC core (Figs. 5c,g). In the TC inner core, a complete ring of nearly saturated air, associated with the TC eyewall, is still intact in the composite of early-RI members (Fig. 5c); however, nearly the entire southeastern quadrant of the late-RI composite is comprised of relative humidity $< 50\%$ (Fig. 5g). The degradation of the inner-core moisture in late-RI members around 36 h into the simulations occurs in conjunction with the collapse of the eastern eyewall, as seen in simulated radar reflectivities in Fig. 2g and a decrease in TC intensity (Fig. 1). Relative humidity differences between early- and late-RI members at this time exceed 40% in a cyclonically curved band on the south side of the TC, extending outward from the eyewall (Fig. 5k), within the inflow region. Finally, at 48 h into the forecast period, the dry-air intrusion has abated, with the inner-core regions of both ensemble groups showing symmetric rings of $>80\%$ relative humidity observed throughout the innermost 50 km (Figs. 5d,h). Although late-RI members are still associated with a region of statistically significant lower relative humidity, this region is mostly confined to locations radially outward of 50 km (Fig. 5l).

The overlap of the azimuthal location of the dry-air intrusion with the midtropospheric inflow implies radial ventilation of the TC warm core with low-entropy, environmental air (e.g., Tang and Emanuel 2010, 2012; Alland et al. 2021b). Here, radial ventilation was quantified following a method similar to Alland et al. (2021b):

$$\Lambda_u = \rho u' \theta_e', \tag{1}$$

where ρ is the density of air, u is the storm-relative radial wind, θ_e is the equivalent potential temperature, and the prime superscript denotes a perturbation from the azimuthal mean. Regions where both u' and θ_e' are <0 (and thus Λ_u is >0) act to inject the TC warm core with low-θ_e air, providing "antifuel" to the TC heat engine (Tang and Emanuel 2010). The spatial pattern of 400-hPa Λ_u is shown in 3-h increments in Fig. 6, focusing on the period when the dry-air intrusion was quickly approaching the TC core and the intensities of early- and late-RI members began to rapidly diverge.

Figure 6 shows both early- and late-RI members experience a large region of positive Λ_u at 400 hPa, collocated with the upshear inflow of dry air seen in Fig. 5. At 24 h into the

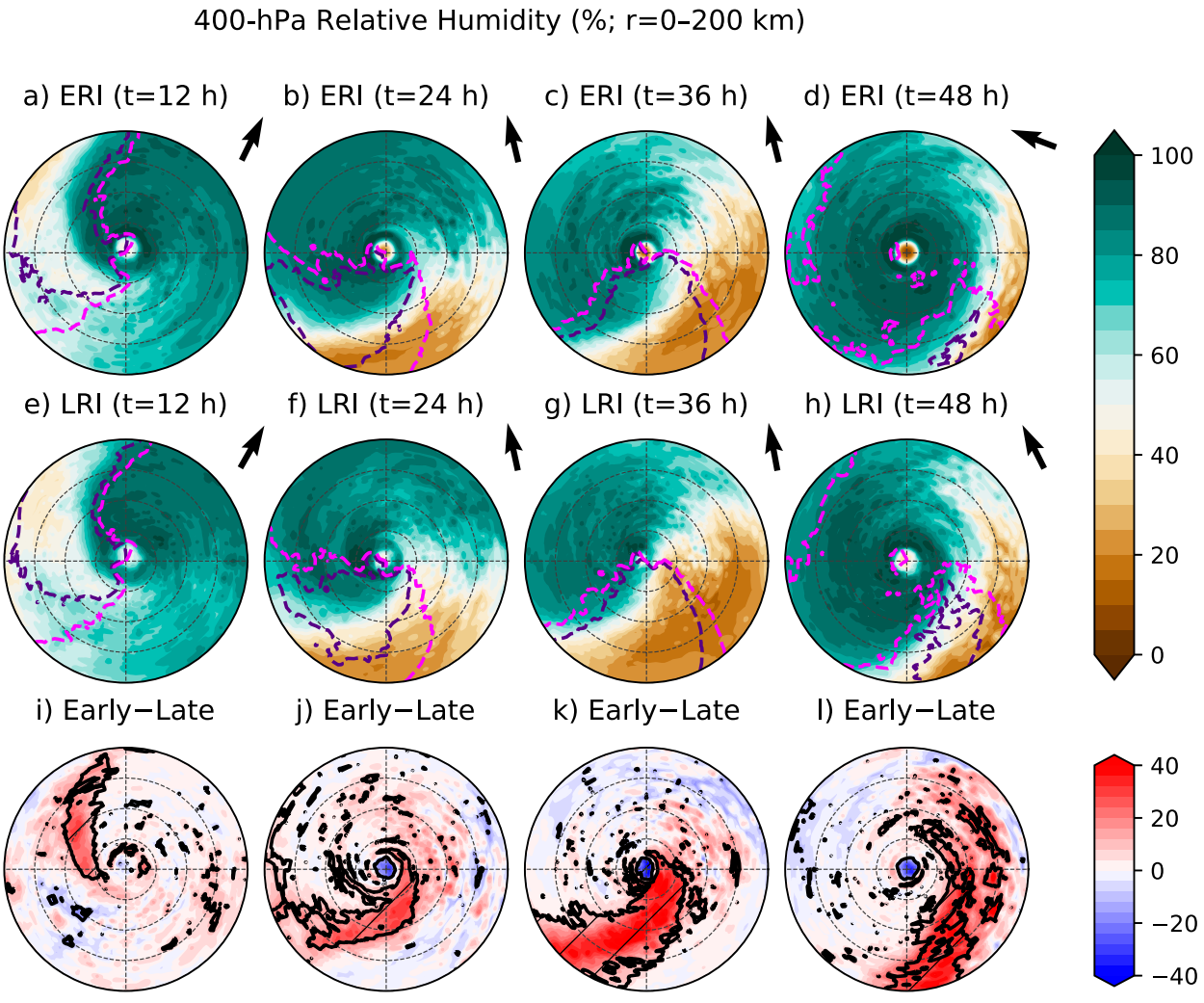

FIG. 5. Storm-centered, 0–200-km, composite-mean, 400-hPa relative humidity (shaded; %) (top) for early-RI members and (middle) late-RI members. Dashed radial rings are spaced in 50-km increments. Storm-relative, 400-hPa radial inflow ≥ 2.5 m s^{-1} is shown by the dashed magenta contours, while inflow ≥ 5 m s^{-1} is shown by the dashed purple contours. The 850–200-hPa shear direction is shown by the black vectors. (bottom) As in the top panels, but for the RH difference between early-RI minus late-RI members. Regions of statistically significant differences are shown by the black contours and hatching. Composites are shown at (a),(e),(i) 12; (b),(f),(j) 24; (c),(g),(k) 36; and (d),(h),(l) 48 h into the simulations.

forecast, significant differences in Λ_u between the two ensemble groups are minimal (Fig. 6i). Shortly thereafter, the dry-air intrusion continues to advance toward the TC center, as Λ_u increases within the upshear region for both early- and late-RI members (Figs. 6b,f). At forecast hour 30, the late-RI composite shows a coherent area of positive Λ_u extending from radii > 200 km wrapping inward toward the TC eyewall (Fig. 6g). The spatial extent and magnitude of the radial ventilation at this time are significantly greater in late-RI members across a swath that extends outward from the TC eyewall to a radius of at least 200 km (Fig. 6k). Although early-RI members do show an uptick in Λ_u at forecast hour 33, radial ventilation remains significantly greater in late-RI members (Figs. 6d,h,l). As a result, it appears plausible the more robust radial ventilation in late-RI members may have eroded upshear inner-core convection, resulting in the asymmetric convective structure seen in Fig. 2f and, ultimately, a reduction in TC intensity (Fig. 1).

To quantify the impact of the dry-air intrusion on the thermodynamic state of the TC core, a column-integrated moist static energy (MSE) budget was computed for a representative early-RI and late-RI member (the same members shown in Fig. 2). MSE provides a desirable framework to examine the impacts of ventilation on TC convective processes as column-integrated MSE is approximately conserved under moist adiabatic motions. Previous studies such as Chen et al. (2019) have identified that a decrease in ventilation facilitates an increase in column-integrated MSE and a moistening of the TC core, which precedes RI onset. The vertically integrated MSE

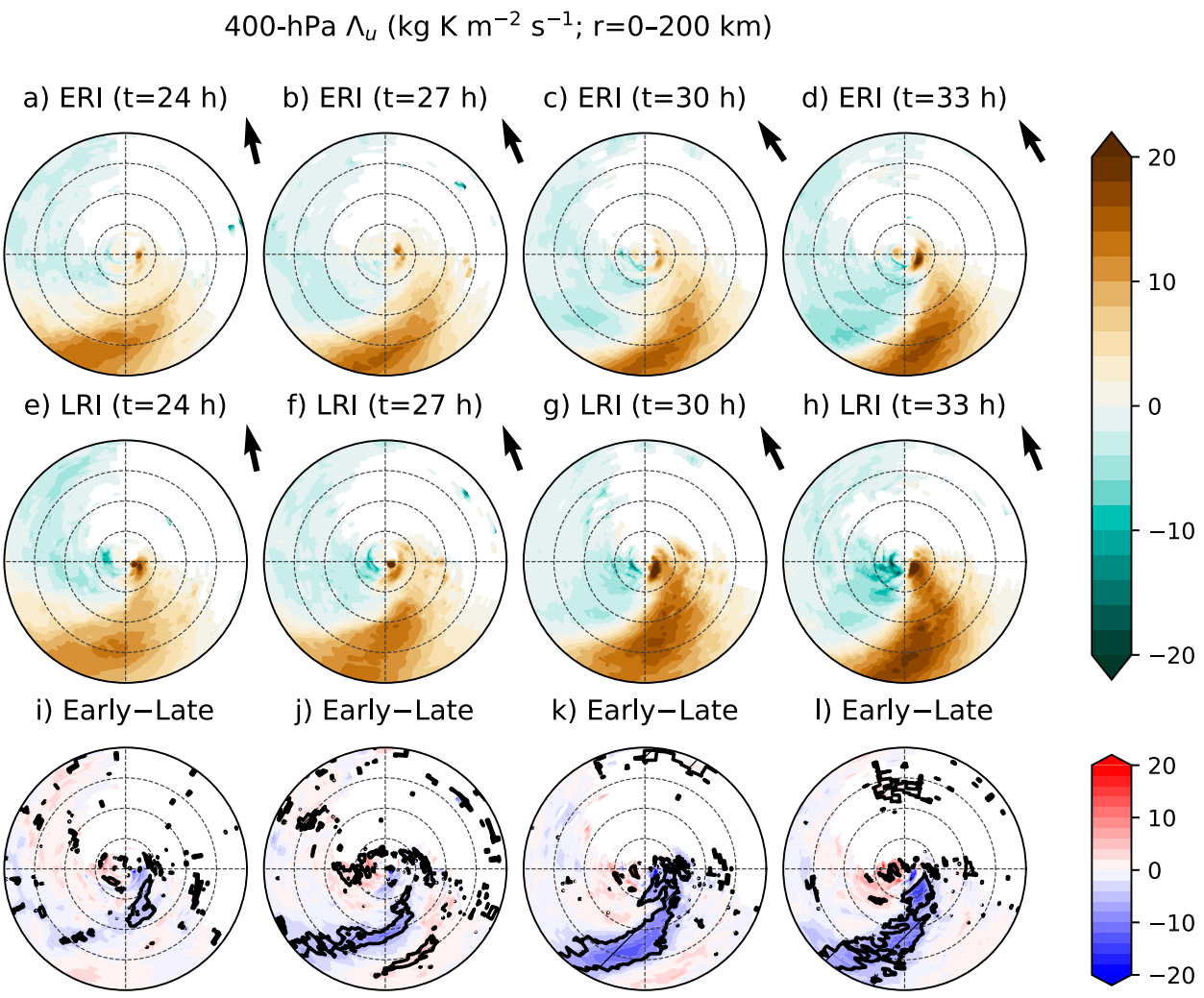

FIG. 6. Storm-centered, 0–200-km, 400-hPa composite-mean radial ventilation (Λ_u; shaded; kg K m^{-2} s^{-1}) (top) for early-RI members and (middle) late-RI members. Dashed radial rings are spaced in 50-km increments. The 850–200-hPa shear direction is shown by the black vectors. (bottom) As in the top panels, but for the difference between early-RI minus late-RI members. Regions of statistically significant differences are shown by the black contours and hatching. Composites are shown at (a),(e),(i) 24; (b),(f),(j) 27; (c),(g),(k) 30; and (d),(h),(l) 33 h into the simulations.

budget follows Sobel et al. (2014) and Chen et al. (2019) and is given by

$$\left\langle \frac{\partial (c_p T + L_v q)}{\partial t} \right\rangle = -\langle \mathbf{u} \cdot \nabla (c_p T + L_v q) \rangle - \left\langle \omega \frac{\partial h}{\partial p} \right\rangle + \text{SFX} + \left\langle c_p \left(\frac{\partial \theta}{\partial t} \right)_R \right\rangle, \quad (2)$$

where h denotes MSE ($h = c_p T + gz + L_v q$), c_p is the dry air heat capacity at constant pressure, T is temperature, L_v is the latent heat of vaporization (treated as a constant value of 2.5×10^6 J kg^{-1}), q is specific humidity, and $\mathbf{u}$ is the horizontal velocity. SFX indicates surface fluxes of enthalpy, including both sensible and latent heat fluxes. The final term, $c_p(\partial\theta/\partial t)_R$, denotes radiative heating or cooling from both longwave and shortwave radiation. Angle brackets indicate the values are mass-weighted vertical integrals from 900 to 100 hPa.[3] Similar to Neelin (2007) and Chen et al. (2019), the MSE budget shown in (2) uses moist enthalpy ($c_p T + L_v q$) rather than h in the time tendency and horizontal advection terms, as this was found to lead to a better closure of the MSE budget. Although the left-hand side of (2) omits the gz term in h, variations in gz were relatively small and often out of phase with changes in h. In this study, all MSE budget terms are

[3] The 900–100-hPa layer was selected to represent a near-tropospheric deep column considering the relatively intense TCs examined here, while also accounting for differences in TC intensity between early-RI and late-RI members. If a surface–100-hPa integral was used instead, such as in Chen et al. (2019), differences in the column-integrated mass between early-RI and late-RI members would affect the interpretation of the MSE budget.

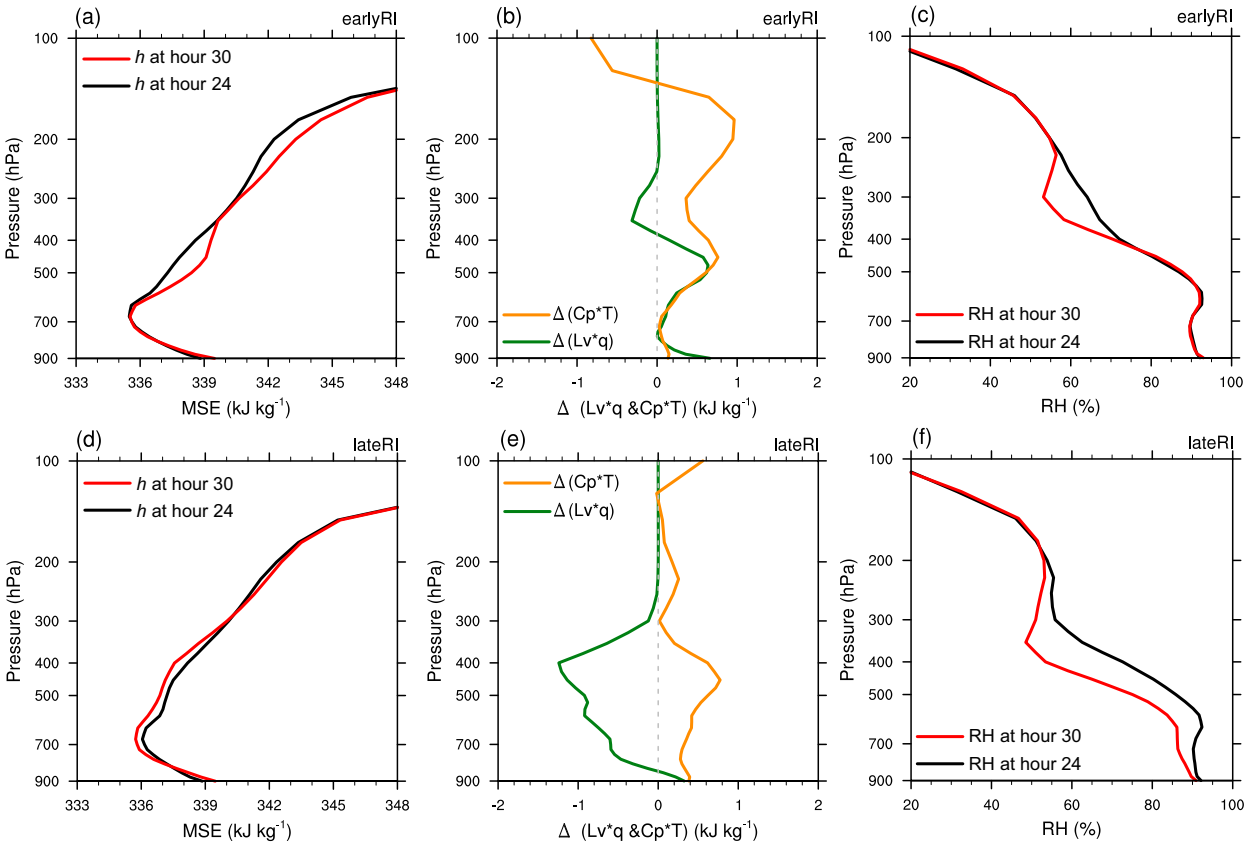

FIG. 7. (a) Vertical profiles of moist static energy (h or MSE; kJ kg^{-1}) for the representative early-RI member at forecast hours 24 (black line) and 30 (red line). Profiles are derived from domain-averaged values within a 240 km × 240 km TC-centered box. (b) Vertical profiles of the change in c_pT (orange line; kJ kg^{-1}) and L_vq (green line; kJ kg^{-1}) between forecast hours 24 and 30. Positive values denote increases with time. (c) As in (a), but for profiles of relative humidity (RH; %). (d)–(f) As in (a)–(c), but for the representative late-RI member.

shown in the form of domain averages within a 240 km × 240 km TC-centered box. This domain size was selected to represent mesoscale changes within the TC core region and sensitivity tests using slightly different domain sizes yielded similar results. Finally, the effects of the SFX and $\langle c_p(\partial\theta/\partial t)_R\rangle$ terms in (2) are not shown in the subsequent analyses because surface fluxes and radiation were not stored within the ensemble output; however, these terms tend to act as sources of MSE (Chen et al. 2019) and are not necessary to assess how ventilation processes affect column-integrated MSE.

To provide context for the column-integrated MSE budget, Figs. 7a and 7d show domain-averaged vertical profiles of MSE at forecast hours 24 and 30. This temporal window focuses on the period when radial ventilation was becoming increasingly pronounced (Fig. 6). During this period, the late-RI member experienced a slight decrease in MSE throughout much of the midtroposphere, between approximately 800 and 300 hPa. This decrease in MSE stands in contrast to the early-RI member which experienced an increase in tropospheric MSE above 600 hPa, with the exception of a layer between approximately 400 and 300 hPa. In the early-RI member, both internal energy (c_pT) and latent heat (L_vq) increased over much of the troposphere—besides a small reduction in latent heat between 400 and 300 hPa—indicating the dry-air intrusion did not significantly alter the local thermodynamic state of the early-RI member (Fig. 7b). The evolution of the late-RI member differed starkly (Fig. 7e), with evidence of mesoscale subsidence reflected by an increase in internal energy (or column warming) and a decrease in latent heat (or column drying) maximized near the height of the dry-air intrusion shown in Fig. 5. Consistent with the drying and warming associated with mesoscale subsidence, domain-averaged relative humidity in the late-RI member decreased by approximately 10%–15% over a deep layer, between 600 and 350 hPa (Fig. 7f).

The evolution of the column-integrated MSE budget results is shown in Fig. 8. Although the early-RI and late-RI member display similar column-integrated values of moist enthalpy at forecast hour 22 (Fig. 8a), the members begin to quickly diverge, with the late-RI member featuring a decrease over the next 6–8 h. Decomposing moist enthalpy into internal energy and latent heat shows that the late-RI member's loss of MSE was driven by a drying of the column despite an increase in the internal energy, which is consistent with the effects of mesoscale subsidence discussed earlier (Fig. 8b). Meanwhile, the early-RI member experienced minimal changes in latent heat, demonstrating the ventilation episode was much more

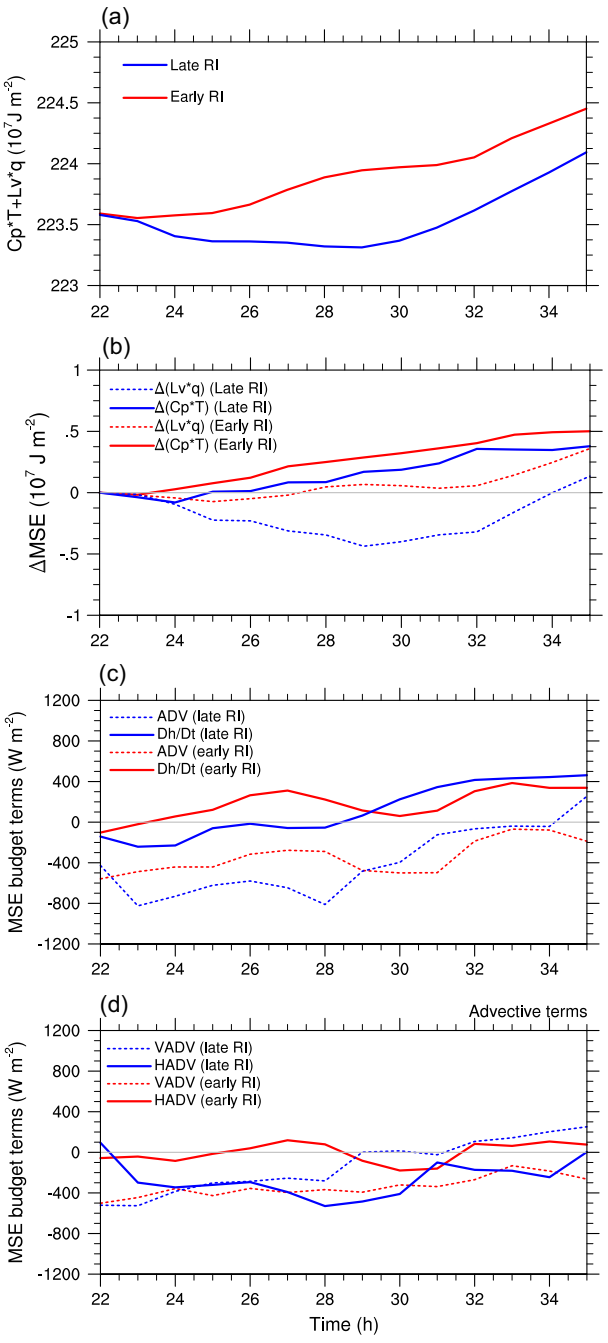

FIG. 8. (a) Time series of domain-mean $c_pT + L_vq$ (10^7 J m^{-2}) for the representative early-RI member (red) and late-RI member (blue). Here, values are averaged within a 240 km × 240 km TC-centered box. (b) Time series of the change in internal energy (c_pT; 10^7 J m^{-2}; solid line) and latent heat (L_vq; 10^7 J m^{-2}; dashed line) relative to their values at forecast hour 22. Red and blues lines denote the representative early-RI and late-RI member, respectively. (c) As in (a), but for select MSE budget terms (W m^{-2}). Here, the time tendency of h is shown by the solid lines, while the sum of the horizontal and vertical advection terms is shown by the dashed lines. (d) As in (a), but for select MSE budget terms (W m^{-2}). Here, the horizontal advection of h is shown by the solid lines, while the vertical advection of h is shown by the dashed lines.

detrimental in the late-RI member. The time derivative of MSE for both members can be more clearly seen in Fig. 8c. The late-RI member progressively loses column-integrated MSE until forecast hour 29 as the dry intrusion approaches, whereas the early-RI member gained MSE at nearly all times shown in Fig. 8c.

Interestingly, the sum of the advection terms (dashed lines in Fig. 8c) vary in phase with the MSE tendency in both early-RI and late-RI member, demonstrating the key role of advective processes in modulating the column-integrated MSE. In the late-RI member, a substantial loss of MSE due to advection is evident, with rates that approach −800 W m^{-2} between forecast hours 22 and 28. Alternatively, although the sum of MSE advection is also negative in the representative early-RI member over this period, the loss of MSE through advection in the early-RI member is approximately half the rate of the late-RI member. Figure 8d indicates the loss of MSE in the late-RI member is primarily driven by horizontal advection after forecast hour 28. Curiously, the loss of column-integrated MSE due to vertical advection is actually larger in the early-RI member as the dry-air intrusion approaches the TC core. Considering previous studies have hypothesized radial ventilation can result in the downward transport of low-entropy air into the boundary layer (Tang and Emanuel 2010; Riemer and Montgomery 2011; Alland et al. 2021b; Alland and Davis 2022), the weaker depletion of MSE due to vertical advection in the late-RI member warrants further investigation.

Figures 9 shows the vertical structure and evolution of the vertical advection of MSE. It is important to recall that the vertical profile of MSE features a pronounced midtropospheric minimum near 600 hPa in these simulations (Figs. 7a,d), consistent with climatological profiles of equivalent potential temperature in moist tropical environments (Ooyama 1969; Dunion 2011). Thus, the vertical advection of MSE from mesoscale ascent acts to increase MSE below the midtropospheric MSE minimum and decrease MSE above the midtropospheric MSE minimum (e.g., Chen et al. 2019). Conversely, regions of mesoscale descent act to decrease MSE below the midtropospheric MSE minimum and increase MSE above the midtropospheric MSE minimum. In the early-RI member, a pattern of mesoscale ascent is displayed at all times shown in Fig. 9a. Interestingly, in the late-RI member, regions of positive vertical advection of MSE are seen above the midtropospheric MSE minimum after forecast hour 28 (Fig. 9b). This pattern indicates the presence of mesoscale subsidence in the mid- to upper troposphere, consistent with the warming and drying seen in Fig. 7e. The mesoscale subsidence above the midtropospheric MSE minimum acts to increase MSE by bringing down relatively large values of MSE from the upper-troposphere, despite resulting in a decrease in humidity (Figs. 7e,f).

Nevertheless, the drying of the core region in the late-RI member (Fig. 7f) is consistent with the decrease in the column-integrated MSE or moist enthalpy (Fig. 8a) over the period of hours 24–30. The core region in the late-RI member starts to rapidly accumulate MSE and moisture afterward (Figs. 8a,b), which precedes the onset of RI approximately six hours later. This result is consistent with Chen et al. (2019) and emphasizes the importance of a near-saturated core

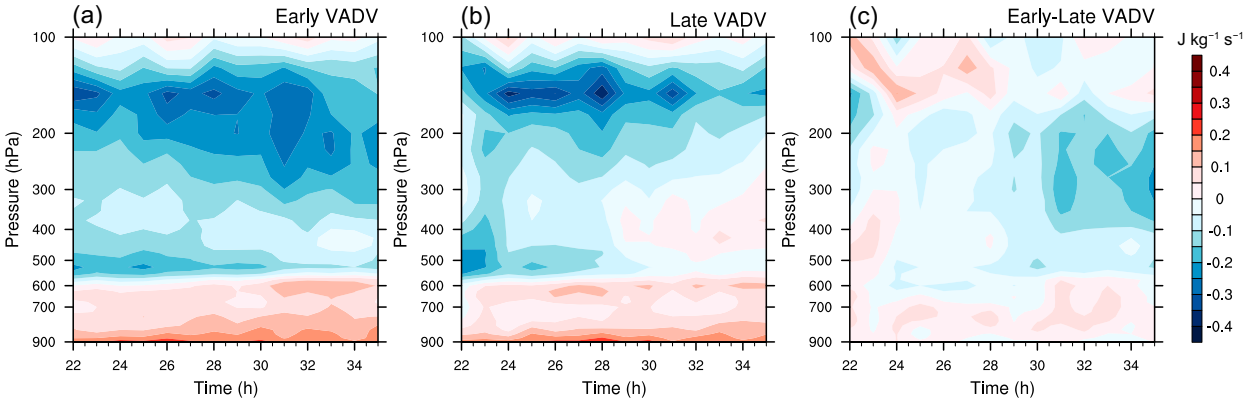

FIG. 9. (a) Time series of the vertical structure of the vertical advection term of the MSE budget (J kg^{-1} s^{-1}) for the representative early-RI member. (b) As in (a), but for the representative late-RI member. (c) Difference in vertical advection of MSE of the representative early-RI member minus the late-RI member.

(e.g., Figs. 3 and 5) for sustained TC convective activity and intensification.

Last, the vertical advection of MSE near the top of the TC boundary layer was similar for the representative early- and late-RI member (between 900 and 850 hPa in Fig. 9c), suggesting the greater radial ventilation experienced by the late-RI member did not result in appreciably greater downdraft ventilation into the boundary layer. On the contrary, the late-RI member displayed an increase in moist enthalpy between 900 and 850 hPa (Fig. 7e). Nevertheless, mesoscale subsidence in the representative late-RI member did result in a pronounced drying of the troposphere above the boundary layer, revealing a pathway through which radial ventilation can significantly alter the thermodynamic state of the TC core without appreciably modifying the thermodynamic characteristics of the TC boundary layer. The response of the TC vortex and convective structures to this episode of radial ventilation will be explored in the next sections.

5. A tale of two vortex evolutions

a. *Vortex tilt*

To evaluate the impacts of the ventilation episode on the structure of the TC vortex, Fig. 10a shows time series of the

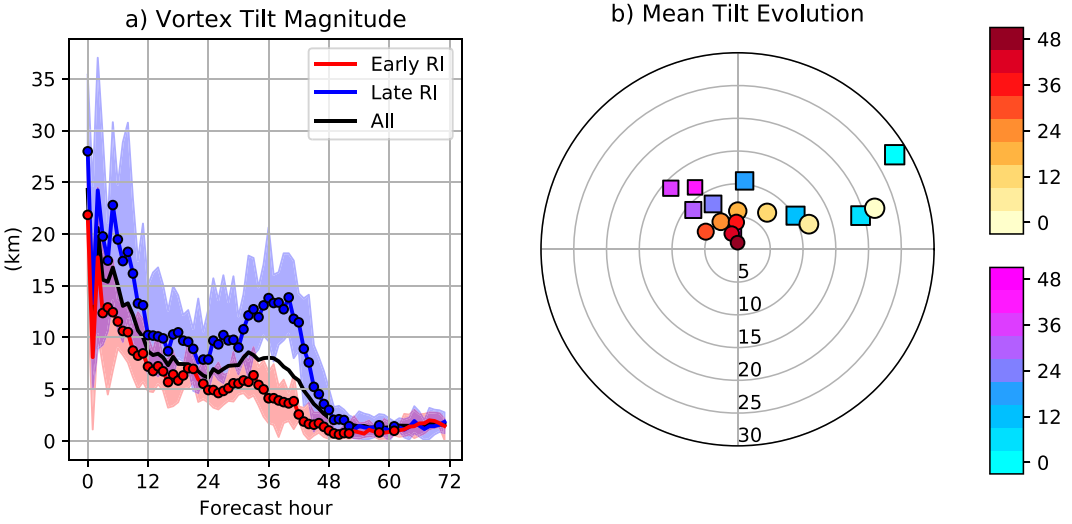

FIG. 10. (a) Composite-mean ensemble forecasts of surface–400-hPa vortex tilt magnitude (km) for early-RI members (red), late-RI members (blue), and all ensemble members (black). Red-shaded regions span the entire distribution of early-RI members, while blue-shaded regions span the distribution of late-RI members. Dotted points denote times where the differences between early and late-RI members are statistically significant at the 95% confidence level. (b) Mean orientation of the surface–400-hPa vortex tilt configuration for early-RI members (circles; warm colors) and late-RI members (squares; cool colors). Vortex tilt is shown in 6-h increments beginning at forecast hour zero and ending at forecast hour 48 (shaded). The vortex tilt is shown with respect to its geographic heading, where north points toward the top of the figure. Radial rings are spaced in 5-km increments.

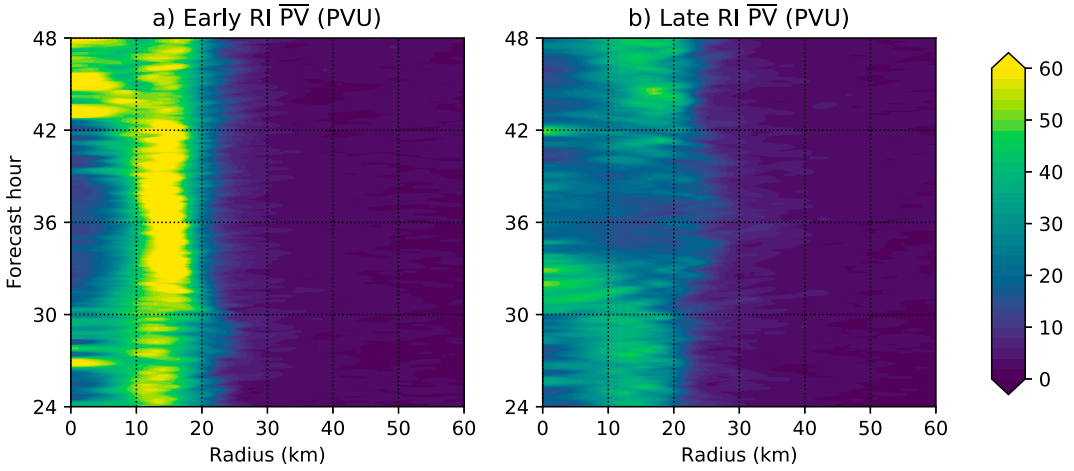

FIG. 11. (a) Time–radius diagram of azimuthally averaged 850-hPa PV (PVU) for the representative early-RI (ERI) ensemble member and (b) late-RI (LRI) ensemble member.

distributions of surface–400-hPa vortex tilt magnitudes for early-RI and late-RI simulations. Here, the upper-level vortex centers were determined by the centroid of geopotential height anomalies within a TC-centered disc with a radius of 100 km, similar to Nguyen et al. (2014). The surface–400-hPa tilt is shown here, as this layer contained the largest differences between early- and late-RI members.

Within the first 24 h of the simulations, both early- and late-RI members are associated with qualitatively similar tilt evolutions, as the magnitude of tilt steadily decreases with time following the noisy initialization spin-up (Fig. 10a). Nonetheless, early-RI members are consistently associated with smaller mean tilt magnitudes than late-RI members, although some overlap in the distributions of tilt magnitude are observed. Following forecast hour 24, pronounced differences in the magnitude of vortex tilt emerge. While early-RI members maintain mean tilt magnitudes near 5 km, late-RI members experience an increase in tilt, with the mean tilt magnitude approaching 15 km by 36 h into the forecast. Although a tilt magnitude of 15 km may appear physically insignificant, the radius of maximum wind of the simulated TCs is approximately 20 km (shown later), indicating that the compact vortices in late-RI members strongly deviate from alignment. Interestingly, the increase in vortex tilt magnitude in the late-RI group occurs near the time when the simulated vortices were subject to an increase in radial ventilation (Figs. 6 and 8) and precedes a period of weakening (Fig. 1). This result suggests the vortex tilt evolution has an important relationship with TC intensity change, which agrees with previous studies (Zhang and Tao 2013; Munsell et al. 2017; Chen et al. 2018b; Rios-Berrios et al. 2018; Alvey et al. 2020; Rios-Berrios 2020; Schecter and Menelaou 2020).

Around 42 h into the forecast period, late-RI members experience a significant decrease in tilt, with magnitudes comparable to early-RI members by forecast hour 48 (Fig. 10a). This shift toward a more aligned vortex in the late-RI members follows a reduction in vertical wind shear magnitude (Fig. 3a) and a recovery of column-integrated MSE (Fig. 8), and also precedes the onset of RI (Fig. 1).

Despite the significantly different tilt magnitude evolutions between the ensemble groups, the evolution of tilt direction for early- and late-RI members are quite similar (Fig. 10b). In both groups, the vortex tilt is consistently downshear-left of the deep-layer shear vector (Fig. 3b), which has been shown to be a preferred tilt configuration in both model simulations and observations (Jones 1995; Reasor et al. 2004, 2013; Fischer et al. 2022). Although a left-of-shear vortex tilt direction minimizes the net vertical shear associated with the superposition of the environmental flow and the cyclonic flow of the misaligned TC circulation (e.g., Jones 1995; Reasor et al. 2004), diabatic processes contribute the actual tilt direction (Davis et al. 2008b), which is often that of a downshear-left orientation.

These results demonstrate vortex tilt magnitude is a consistent differentiating factor between the early- and late-RI groups throughout much of the first 48 h of the simulations, especially during the times of the greatest intensity differences. The increase in the tilt magnitude of late-RI members between forecast hours 30 and 36 occurs in tandem with an uptick in radial ventilation associated with the aforementioned dry-air intrusion (Fig. 6). We hypothesize that the larger vortex tilts in late-RI members aided differential advection of dry, midtropospheric air originating upshear and uptilt of the TC vortex directly over the lower-tropospheric TC center. The implications of such a process on TC intensity change will be explored in later sections.

b. *Horizontal vortex structure*

In addition to pronounced differences in the vertical vortex structure of early- and late-RI members, the two groups displayed marked differences in the evolution of the horizontal vortex structure. Figure 11 shows Hovmöller diagrams of azimuthally averaged, 850-hPa PV for the same representative early-RI and late-RI ensemble members in Fig. 2. Throughout

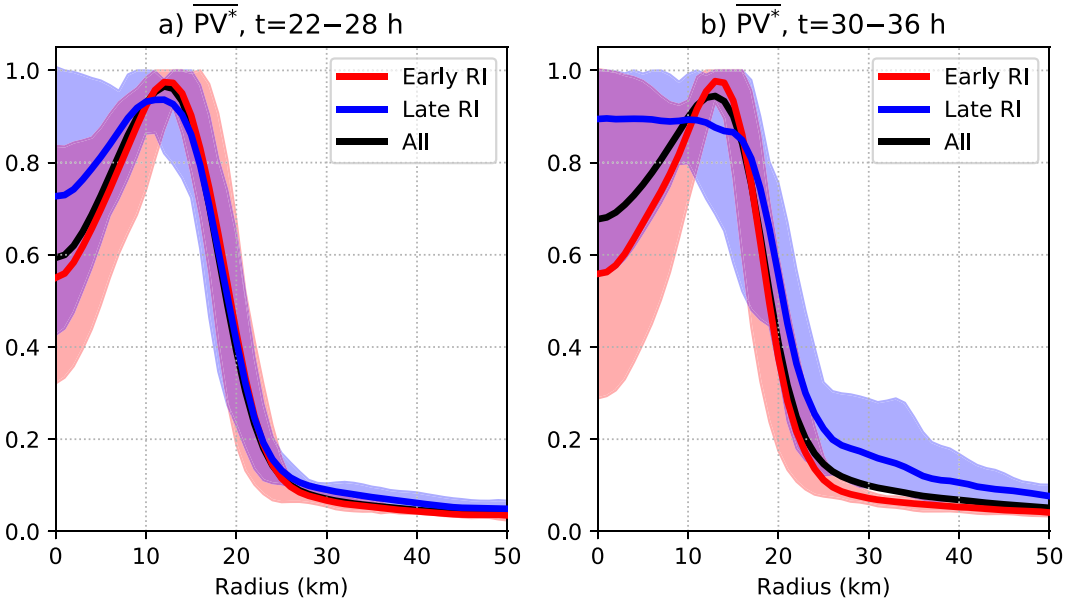

FIG. 12. (a) Composite-mean ensemble forecasts of normalized 850-hPa PV ($\overline{PV^*}$; dimensionless) for early-RI members (red), late-RI members (blue), and all ensemble members (black). Here, $\overline{PV^*}$ is computed by first calculating the time-averaged PV over a period of 22–28 h into the forecast. Next, the azimuthally averaged PV in each radial bin is divided by the maximum azimuthally averaged PV in the entire radial profile. Red-shaded regions span the entire distribution of early-RI members, while blue-shaded regions span the distribution of late-RI members. (b) As in (a), but for forecast hours 30–36.

the majority of the 24–48-h forecast window, the early-RI member is characterized by a ring of higher PV, maximized at a radius of approximately 15 km (Fig. 11a). Such a vortex structure has been shown to be associated with intensifying TCs (Kossin and Eastin 2001; Rogers et al. 2013; Martinez et al. 2017; Hardy et al. 2021).

On the contrary, the representative late-RI vortex is already weaker by forecast hour 24 and displays a vortex morphology that transitions from a ring-like maximum in PV toward a PV monopole shortly after forecast hour 30 (Fig. 11b). By forecast hour 36, the radial gradient of PV in the late-RI member weakens as a secondary maximum of high-PV air propagates outward, seen within the radial band between 20 and 30 km. The weakening of the radial PV gradient as the vortex transitions toward a monopolar structure is consistent with a vortex mixing event (e.g., Schubert et al. 1999; Rozoff et al. 2009). Eventually, the late-RI member transitions back toward a ring-like PV profile following forecast hour 42, near the time of RI onset (Fig. 1).

Evidence supporting the vortex mixing signal across late-RI members is provided in Fig. 12. Here, the azimuthally averaged 850-hPa PV has been normalized by the maximum value in the radial profile in each simulation to account for differences in vortex intensity. Figure 12a shows that between forecast hours 22 and 28, both early- and late-RI members tend to have an annular PV structure, with maximum PV in the radial profile found at radii between 10 and 15 km. By forecast hours 30–36, early-RI members generally maintain a ring-like horizontal PV structure, while late-RI members are associated with significantly greater normalized PV near the TC center and at radii > 25 km (Fig. 12b). The weakening of the radial PV gradient is visible in all late-RI members, suggesting vortex mixing events were an inherent characteristic of the late-RI group during the period when these members experienced an uptick in radial ventilation, grew increasingly tilted, and weakened.

c. *Evolution of vortex resiliency*

The results presented thus far point to a pause in intensification of late-RI members coinciding with a period of prolonged vortex tilt growth, leading to vastly different vortex evolutions when compared to early-RI members. The increasing vortex tilt and associated enhancement of midtropospheric radial ventilation (Fig. 6) can disrupt the organization and vigor of eyewall convection—which will be explored in more detail in the next section—with implications for the spinup of peak winds in the TC boundary layer (e.g., Smith et al. 2021). Given the potentially important role of vortex tilt in producing this marked difference in intensification, we briefly investigate the vortex resilience (i.e., the intrinsic ability to resist the development of tilt when a misalignment forcing, like vertical wind shear, is applied) of the representative early-RI and late-RI members during this critical period.

The simple linear model for TC vortex resilience, described most recently by Schecter (2015) and Reasor and Montgomery (2015), is employed here. In the absence of vertical wind shear forcing, the linearized, Boussinesq primitive equations simulate the evolution of an initial tilt-like perturbation to a barotropic

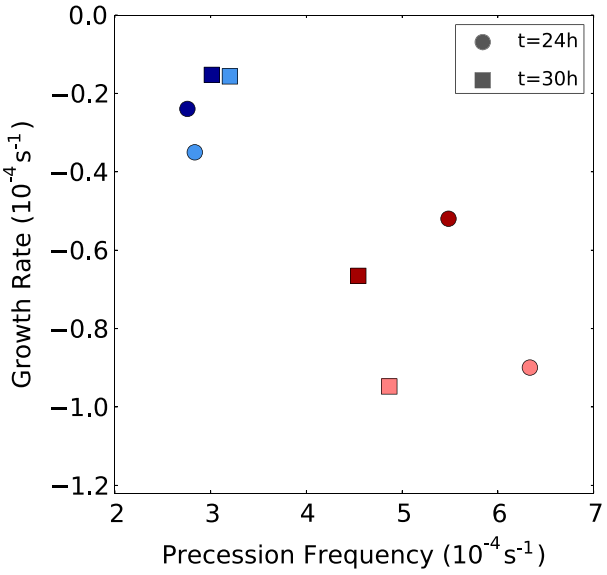

FIG. 13. Scatterplot of the estimated tilt precession frequency (10^{-4} s^{-1}) and growth rate (10^{-4} s^{-1}) for the representative early-RI member (red markers) and late-RI member (blue markers). Analyses at t = 24 h and t = 30 h are shown by the circle and square markers, respectively. The shading of the markers is proportional to the assumed static stability reduction in the eyewall region, where lighter markers indicate less stability.

azimuthal-mean vortex. The mean vortex state is derived from the same representative early-RI and late-RI members shown in previous analyses (e.g., Figs. 2 and 11). Cloudiness in the eyewall region is parameterized using a reduced static stability. Additional details of the model and initialization are described in the appendix. The early evolution of the tilt perturbation for all mean vortex states considered here is controlled by a precessing, damped tilt mode. The mode precession frequency and exponential growth rate (negative values indicate damping) are estimated from time series of the simulated complex radial velocity amplitude (not shown).

Figure 13 summarizes the estimated tilt precession frequency and growth rate for early-RI (red) and late-RI (blue) vortices at forecast hours 24 and 30 for dry and significantly cloudy eyewall conditions. Near the approximate onset of the bifurcation in early-RI and late-RI tilt amplitude evolution at forecast hour 24, the tilt mode of the early-RI vortex precesses a factor of 2 faster and is more strongly damped. For the more intense (Fig. 1) and well-developed eyewall (Fig. 2b) of the early-RI member, the WRF-model vortex resilience is likely more closely approximated by the lower-stability case (i.e., greater cloudiness) from the simple linear model (Schecter 2015). Thus, the less-developed late-RI vortex tilt is damped at nearly one-third the rate of the early-RI vortex. Additionally, in similar vertical wind shear, the late-RI vortex would not be able to precess as readily upshear into a more favorable configuration, making it, overall, less resilient. Six hours later, the late-RI member—as the vortex is further ventilated (Figs. 6g and 7d–f) and the core PV begins its transition from a ring to monopole structure (Fig. 11c)—shows a further decrease in damping rate magnitude. The low-stability case for the early-RI member decreases somewhat in precession frequency, but remains substantially more resilient in terms of damping rate.

Broadly, these differences in the early-RI and late-RI vortex resilience described by the simple linear model are consistent with, and perhaps help explain, the differences in tilt evolution illustrated in Fig. 10. More specifically, the late-RI member exhibits decreasing resilience during the period where the vortex is subject to an increase in ventilation and a disruption of inner-core organization (Figs. 2f,g and 6e–h), which precedes a period of tilt amplification (Fig. 10a). Alternatively, this analysis reveals the early-RI member maintains a more resilient vortex structure, consistent with the observed vortex tilt evolution. We hypothesize the greater resilience of early-RI members was aided by their greater intensity (Fig. 1) and stronger radial vorticity gradient near the tilt-mode critical radius, when compared to late-RI members (Schecter and Montgomery 2003; Reasor et al. 2004; Schecter 2008; Reasor and Montgomery 2015).

6. Convective differences between early- and late-RI members

a. *Overview of azimuthally averaged vertical velocity*

To explore how the different TC vortex evolutions in early- and late-RI members were related to changes in the TC convective structure, Fig. 14 shows 12-h snapshots of the composite-mean, azimuthally averaged vertical velocity ($V_\omega = dp/dt$). Early-RI members are associated with a robust region of sloped ascent ($V_\omega < 0$), associated with the TC eyewall, that increases in magnitude with time (Figs. 14a–d). Additionally, the radial location of peak ascent occurs inward of the radius of maximum tangential wind, which is consistent with observations of intensifying TCs (Rogers et al. 2013; Stevenson et al. 2018; Fischer et al. 2020). Persistent ascent inside the radius of maximum wind has been argued to be an essential characteristic of TC intensification because the associated boundary layer inflow of the TC secondary circulation can advect relatively large angular momentum surfaces inward (Montgomery and Smith 2014; Smith and Montgomery 2015, 2016).

Late-RI members are depicted by a different morphology and evolution of V_ω than early-RI members (Figs. 14e–h). At forecast hour 12, the late-RI composite already has significantly weaker ascent throughout much of the TC eyewall (Figs. 14e,i). Additionally, the late-RI composite contains a double-minimum in V_ω, with a primary minimum at a height of approximately 800 hPa, and a secondary minimum near 300 hPa. By forecast hour 24, the double-minimum structure in V_ω is more apparent, separated by relatively weak ascent in the eyewall between 500 and 400 hPa (Fig. 14f). By 36 h into the simulations, late-RI members experience a reduction in ascent throughout much of the troposphere, with an area of subsidence ≥ 2 Pa s^{-1} between 800 and 450 hPa in the vertical, along the inner edge of the eyewall (Fig. 14g). The ascent in the eyewall at this time is significantly weaker than early-

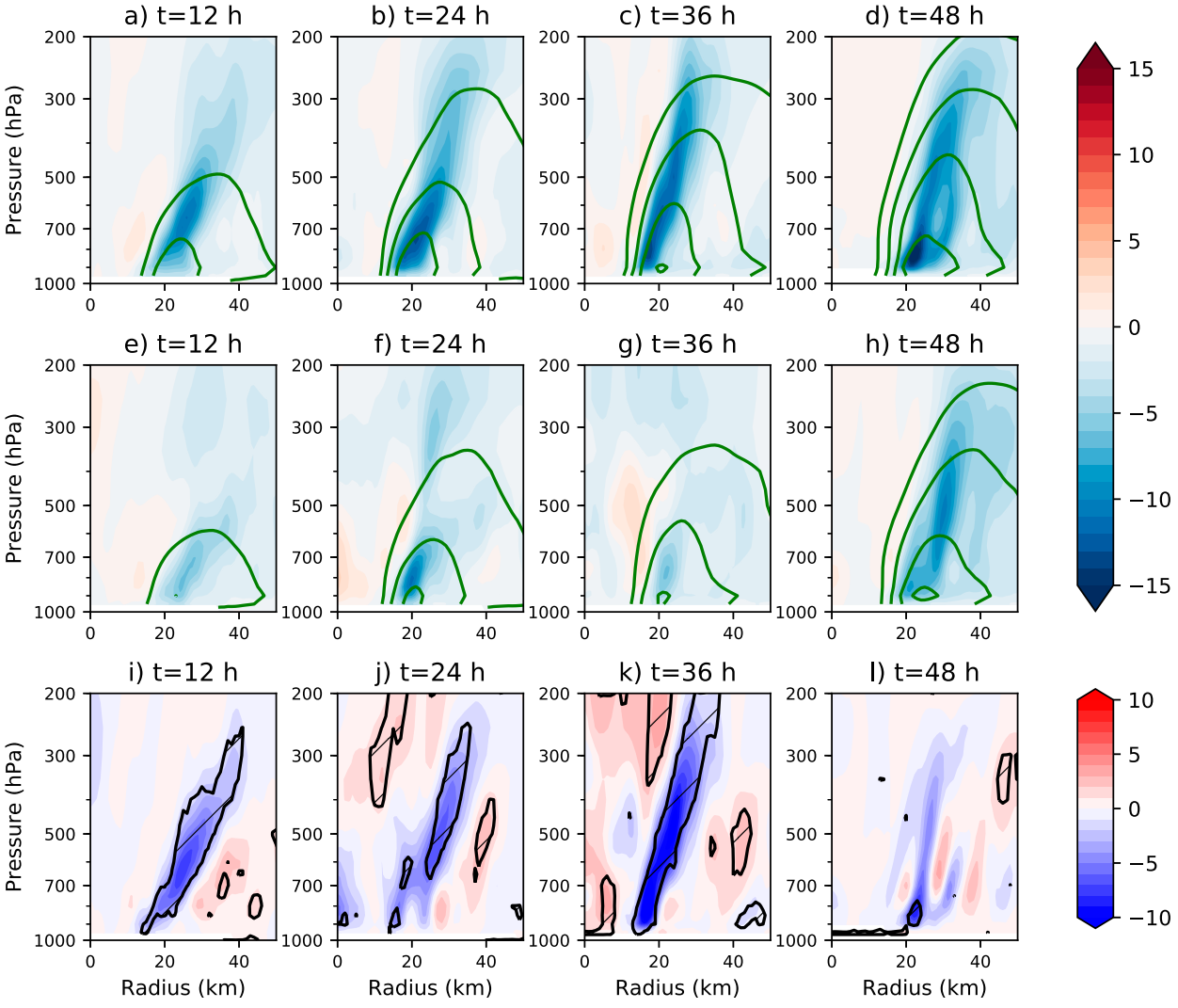

FIG. 14. Storm-centered, azimuthally averaged, composite-mean vertical velocity (V_ω; shaded; Pa s^{-1}) (top) for early-RI members and (middle) late-RI members. Composite-mean, azimuthally averaged tangential wind is contoured in green in 10 m s^{-1} increments, beginning at 30 m s^{-1}. (bottom) As in the top panels, but for the difference in V_ω between early-RI minus late-RI members. Regions of statistically significant differences are shown by the black contours and hatching. Composites are shown at (a),(e),(i) 12; (b),(f),(j) 24; (c),(g),(k) 36; and (d),(h),(l) 48 h into the simulations.

RI members throughout a deep layer (Fig. 14k). This weakening of the TC secondary circulation in late-RI members occurs following the increase in ventilation and vortex tilt (Figs. 6, 8, and 10), supporting the hypothesis that radial ventilation significantly eroded the TC convective structure. By forecast hour 48, however, as the late-RI members begin to undergo RI, the late-RI composite displays a marked increase in ascent throughout the eyewall (Fig. 14h) and differences in V_ω between the two ensemble groups are no longer significant above 800 hPa (Fig. 14l).

b. *Relationship between convective heating and inner-core moisture*

The connection between the midtropospheric dry-air intrusion and the horizontal structure of convective heating is examined in Fig. 15. Here, the composite structure of 400-hPa relative humidity is overlaid onto composite 400-hPa diabatic heating, directly outputted from the model's microphysics scheme. In both ensemble groups, the inner-core convective and moisture fields are characterized by an azimuthal wavenumber-one asymmetry, with regions of heating and moist air located on the western side of the TCs (Figs. 15a–h). A local minimum in relative humidity is found near, and to the northwest of, the TC center, related to subsidence in the tilted TC eye (Fig. 10).

In the early-RI simulations, the azimuthal extent of positive diabatic heating gradually decreases with time, as the region of relative humidity > 75% shrinks (Figs. 15b–d). Additionally, the spatial pattern of diabatic heating becomes increasingly asymmetric, with peak heating occurring left-of-shear and a region of weak diabatic cooling found in the right-of-shear

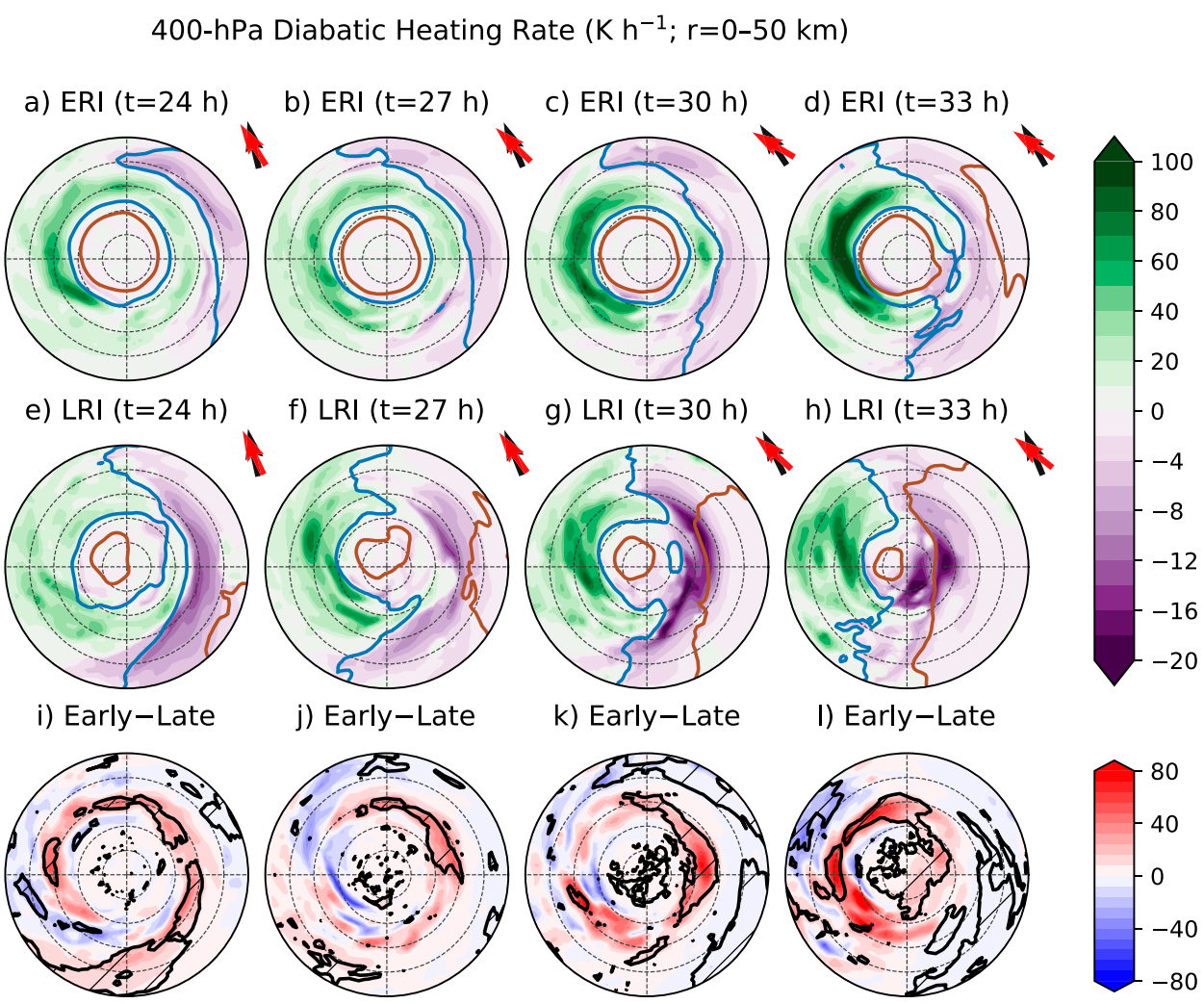

FIG. 15. Storm-centered, composite-mean, 400-hPa instantaneous diabatic heating rate, as directly output from the microphysics scheme (shaded; K h^{-1}) within the innermost 50 km of (top) early-RI members and (middle) late-RI members. Storm-centered, composite-mean 400-hPa relative humidity is contoured at 75% (blue) and 50% (brown). Dashed radial rings are spaced in 10-km increments. The composite 850–200-hPa shear direction and the surface–400-hPa vortex tilt direction are shown by the black and red vectors, respectively. (bottom) As in the top panels, but for the difference between early-RI minus late-RI members. Regions of statistically significant differences in diabatic heating are shown by the black contours and hatching. Composites are shown at (a),(e),(i) 24; (b),(f),(j) 27; (c),(g),(k) 30; and (d),(h),(l) 33 h into the simulations.

quadrants (Fig. 15d). The region of diabatic cooling indicates the evaporation or sublimation of liquid and frozen hydrometeors from the impinging dry air mass.

The composites of late-RI members also display asymmetric diabatic heating, however, the dry-air intrusion reaches closer toward the TC center (Figs. 15e–h). By forecast hour 30, a pronounced band of diabatic cooling in excess of 20 K h^{-1} is found on the eastern, or uptilt, side of the TC, at radii of 10–30 km (Fig. 15g). This increase in diabatic cooling in late-RI members occurs within a sharp moisture gradient, at the leading edge of the dry-air intrusion, and immediately precedes an increase in vortex tilt magnitude (Fig. 10a). Three hours later, the inner-core moisture envelope of late-RI members continues to decay, coincident with an inward progression of the band of diabatic cooling, nearly directly over the lower-tropospheric TC center (Fig. 15h). At this point, the vortex tilt has continued to increase (Fig. 10a) and a significant disruption of the inner-core vortex structure is underway (Fig. 11). These results indicate the inward advancement of the dry-air intrusion in late-RI members acted to disrupt inner-core diabatic heating in the uptilt eyewall through the sublimation and evaporation of hydrometeors in an increasingly dry environment.

7. How do the initial conditions relate to the intensity spread?

Although the TC intensity evolution of this ensemble forecast has been shown to be closely tied to the impacts of a

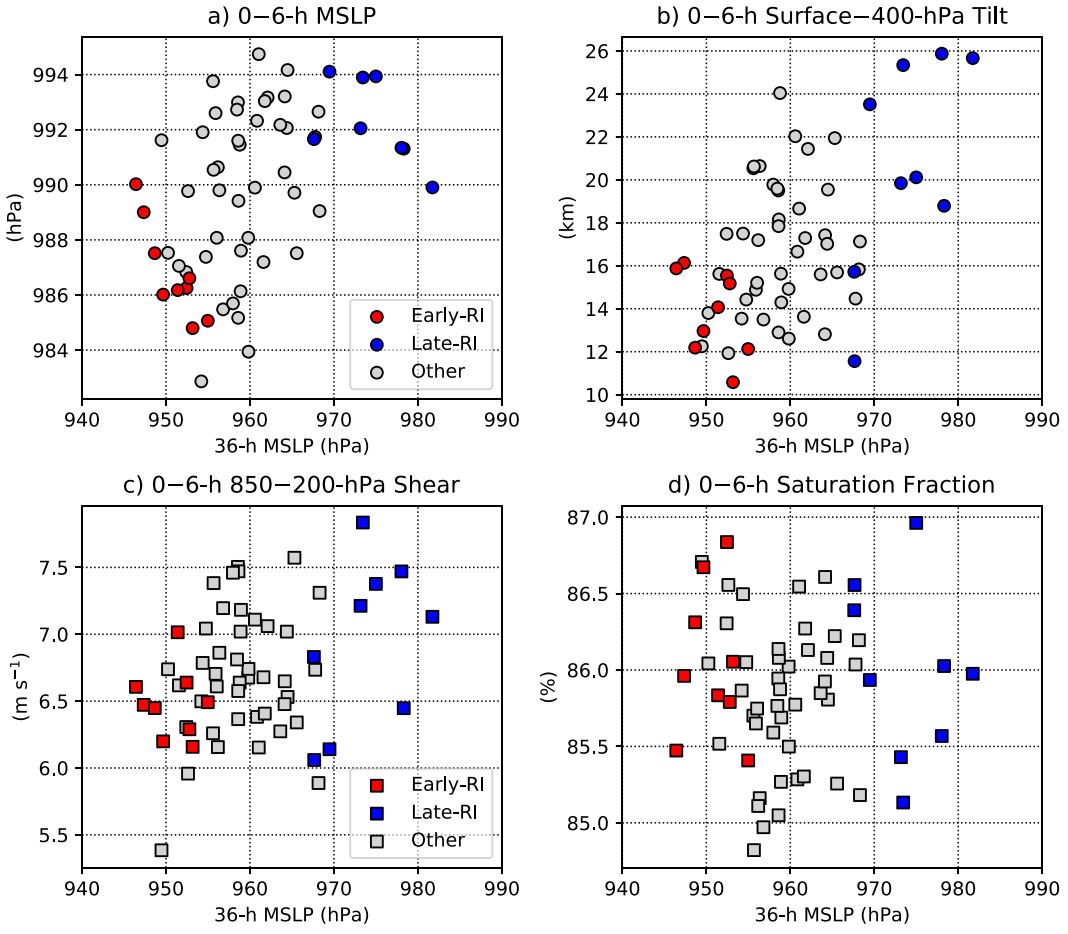

FIG. 16. (a) Scatterplot of the relationship between the minimum central pressure (hPa) at forecast hour 36 and 0–6-h time-averaged minimum central pressure (hPa). Early-RI members are shown in red, late-RI members are shown in blue, and the remaining ensemble members are shown in gray. (b)–(d) As in (a), but for the relationship between the minimum central pressure (hPa) at forecast hour 36 and 0–6-h time-averaged surface–400-hPa tilt magnitude (km), 850–200-hPa shear magnitude (m s^{-1}), and column saturation fraction (%) averaged within the innermost 200 km of the TC, respectively. In each panel, circle markers indicate that the 0–6-h time-mean difference between early- and late-RI members are statistically significant at the 95% confidence level. Square markers indicate the lack of statistical significance.

ventilation episode approximately 24–36 h into the forecast, one question remains: To what extent were the differing intensity evolutions tied to differences in the initial state of each simulation? To briefly address this question, Fig. 16 shows the relationship between time-averaged measures of TC intensity, vortex tilt, vertical wind shear, and inner-core moisture over the first six hours of the simulations and the minimum central pressure at forecast hour 36, when the forecast intensities featured significant spread.

Significant differences in the initial TC intensities and tilt magnitudes between early- and late-RI members were identified. Specifically, early-RI members were associated with significantly greater initial intensities (Fig. 16a) and more aligned vortices (Fig. 16b) than late-RI members. Alternatively, even though early-RI members experienced slightly weaker initial shear magnitudes than late-RI members, with median differences of approximately 0.7 m s^{-1}, the respective distributions display substantial overlap, and the differences in shear were not found to be statistically significant (Fig. 16c). Similarly, measures of the initial inner-core moisture, such as the 0–200-km domain-averaged column saturation fraction (Fig. 16d), featured minimal connections to the TC intensity spread at forecast hour 36. Similar analyses using other inner-core moisture metrics, such as relative and specific humidity at different vertical levels, also yielded no relationship to the subsequent divergence in TC intensity (not shown).

These results suggest that for the present simulations, TC intensity uncertainty is more closely related to differences in the initial TC kinematic structure, including the intensity of the storm, than differences in the initial inner-core moisture field. This finding differs from the results of Emanuel and Zhang (2017), who found intensity forecast error growth is

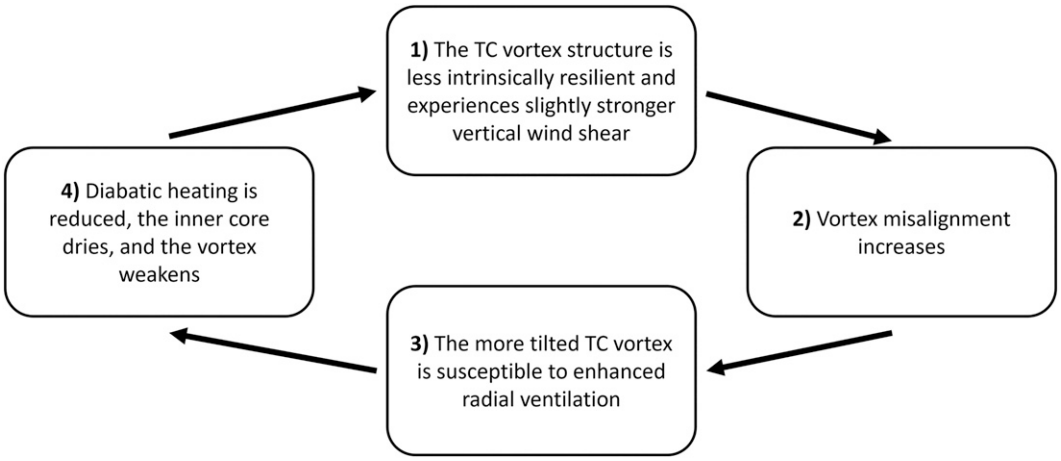

FIG. 17. A flowchart summarizing the feedback experienced by late-RI members during a period of weakening.

quite sensitive to initial inner-core tropospheric moisture. In the present study, significant moisture differences do not begin to emerge until later in the forecast period, as the TC begins interacting with a nearby upper-tropospheric trough and an associated dry-air intrusion as early as 12 h into the forecast period (Fig. 5i). Thus, we hypothesize differences in the TC kinematic structure are important for determining the degree of ventilation TCs experience as they interact with upper-tropospheric troughs or other sources of dry-air intrusions, in agreement with the findings of Riemer and Montgomery (2011), Alland et al. (2021b), and Finocchio and Rios-Berrios (2021).

8. Conclusions

This study examined a 60-member AHW ensemble forecast of Hurricane Gonzalo (2014), which was characterized by a short-term intensity forecast with significant uncertainty as the storm experienced moderate vertical wind shear while interacting with an upper-tropospheric trough. Each ensemble member consisted of the same set of parameterizations, but featured small perturbations to the initial and boundary conditions, on the scale of observational errors. Two groups of unique TC intensity evolutions were studied, which featured an intensity spread of approximately 20 m s^{-1} just 36 h into the forecast. The first ensemble group, labeled early-RI members, experienced RI immediately after initialization. The second group, referred to as late-RI members, experienced more gradual intensification, before temporarily weakening 30–42 h into the forecast period, but rapidly intensified thereafter. Ultimately, the TC intensities of both groups converged by forecast hour 60 as all simulations reached major hurricane intensity. Thus, the significant uncertainty in the short-term intensity was primarily driven by differences in the timing of RI, which has been shown to exhibit decreased predictability in environments of moderate vertical wind shear (Zhang and Tao 2013; Tao and Zhang 2014; Rios-Berrios et al. 2018).

The following list summarizes the key factors that are hypothesized to contribute to the significantly different vortex evolutions of early-RI and late-RI members:

- The weakening of late-RI members was linked to a period of significantly greater ventilation from a mid- to upper-tropospheric dry-air intrusion compared to early-RI members.
- A column-integrated MSE budget analysis for a representative early- and late-RI member revealed the late-RI member experienced a greater loss of MSE within the TC core due in large part to horizontal advection, consistent with the import of low-entropy environmental air from radial ventilation (e.g., Tang and Emanuel 2010; Alland et al. 2021b; Finocchio and Rios-Berrios 2021).
- The greater radial ventilation in the late-RI member was associated with mesoscale subsidence in the TC core, which acted to dry and warm a deep layer of the troposphere underneath the height of the dry-air intrusion, but above the TC boundary layer. Although this subsidence did not reduce MSE within the TC boundary layer as in cases where downdraft ventilation flushes the boundary layer with low-entropy air (e.g., Riemer et al. 2010; Alland et al. 2021a; Chen et al. 2021), late-RI members experienced a significant erosion of diabatic heating in the uptilt and upshear portion of the TC core in an increasingly dry environment.
- Analyses using a linearized primitive equation model showed that as the mid-to-upper-tropospheric dry-air intrusion approached the TC inner core, late-RI members exhibited vortex structures that were intrinsically less resilient and more tilted than early-RI members, while also experiencing slightly stronger shear. As diabatic heating became increasingly asymmetric and the inner core dried, late-RI members displayed decreasing resilience and the vortex became increasingly misaligned. We hypothesize differential advection from the increasingly misaligned vortex facilitated a pathway where low-entropy environmental air could be advected nearly directly over the low-level vortex and late-RI members weakened as part of a feedback loop illustrated in Fig. 17.
- As ventilation reduced diabatic heating within the inner-core of late-RI members, the vortex structure transitioned from a ring-like configuration of enhanced PV toward a PV

monopole. We hypothesize ventilation in the eyewall reduced convectively generated PV beyond the critical value needed to maintain the barotropically unstable, PV-ring configuration (Schubert et al. 1999; Kossin and Schubert 2001; Rozoff et al. 2009). The vortex breakdown event in late-RI members provides evidence of an additional pathway through which ventilation can weaken the TC vortex, as high-PV and high-entropy air were expelled outward from the low-level eyewall, further weakening the TC eyewall front and thereby the intensity of the vortex (Tang and Emanuel 2012).

- TC intensity uncertainty was more closely related to differences in the initial TC kinematic structure than differences in the initial inner-core moisture field. Specifically, early-RI members were associated with initially more intense and vertically aligned vortices than late-RI members. These initial differences amplified with time under the influences of ventilation.

The complex, nonlinear nature of the multiscale interactions examined in this study illustrates how initial condition uncertainty can lead to poor predictability via differences in the timing of RI onset, similar to previous studies (Zhang and Tao 2013; Judt and Chen 2016; Rios-Berrios 2020). The vast spread in the short-term intensity forecasts of the present study highlights the importance of accurate observing and data assimilation systems, as well as accurate parameterization schemes, to mitigate forecast-error growth. Specifically, accurate initializations of TC vortex structure and intensity appear critically important for accurate TC intensity forecasts in environments of moderate shear and ventilation. Additionally, the large forecast uncertainty associated with RI onset advocates for the utility of ensemble and probabilistic frameworks.

Acknowledgments. This study began as part of the first author's Ph.D. thesis at the University at Albany. This project benefited from discussions with Dr. Joshua Alland (NOAA/NWS/National Hurricane Center) and Drs. John Molinari and Casey Peirano from the University at Albany, as well as comments from Dr. George Alvey III during an internal review process. We are grateful for the constructive comments of three anonymous reviewers that helped to strengthen our results and improve the clarity of the manuscript. The authors acknowledge funding support from the Office of Naval Research Tropical Cyclone Rapid Intensification (TCRI) Program under Award ONR-005722. Analysis of WRF-AHW output was aided by the wrf-python library (Ladwig 2017).

Data availability statement. Due to the large file size of the ensemble simulation (~10 TB), data are stored on discs locally at the University of Albany. Select storm-centered model output are available at https://doi.org/10.5281/zenodo.6626422.

APPENDIX

Linearized Primitive Equation Model and Initialization

The linearized primitive equation model and basic configuration used to analyze the tilt modes of vortex profiles derived from the WRF simulations are described by Reasor and Montgomery (2015). We only briefly describe the model and initialization here. The model assumes stably stratified flow (with Brunt–Väisälä frequency $N = 1.15 \times 10^{-2}$ s^{-1}) and employs the Boussinesq and *f*-plane approximations in a cylindrical pseudo-height coordinate system bounded by isothermal rigid lids. The vortex center from the WRF model simulation is used to define the constant Coriolis parameter in each simulation. The equations are linearized about a barotropic mean vortex state derived from representative early-RI and late-RI WRF ensemble members. The mean is defined here by an azimuthal average about the surface vortex center and a vertical average over the 900–250-hPa layer which approximately spans the vortex depth (set at 10 km in the primitive equation model). A centered 4-h time average of 6-min WRF output is used to filter convective-scale fluctuations in the mean vortex profile. The perturbation component of the flow is assumed to have the form of an azimuthal wavenumber-one asymmetry with vertical structure of the first internal baroclinic mode. To simulate the impact of cloudiness on the perturbation evolution, a reduced static stability $\Upsilon(r)N^2$ is introduced in the thermodynamic equation (e.g., Schecter and Montgomery 2007; Schecter 2015; Reasor and Montgomery 2015). The minimum value of Υ is set just inside the radius of maximum wind (RMW), with sensitivity experiments carried out using minimum values from 1 ("dry") to 0.4 ("significantly cloudy").

The intrinsic vortex resilience is analyzed by setting vertical wind shear forcing to zero and initializing the linear model with a quasi-balanced vorticity perturbation having radial structure proportional to the azimuthal-mean vorticity gradient, approximating a tilted vortex. Of interest is how the phase and amplitude of the tilt perturbation evolve with time. In all simulations the radial domain extends out to 1600 km. An analytic function is applied to the vortex profile to ensure that the mean tangential wind decays to zero before reaching the sponge layer starting 50 km from the outer boundary. In all cases the model is integrated out 30 h, which equates to approximately 20–30 orbital periods at the RMW for the mean vortices examined here and the time is sufficient to provide robust characterizations of the tilt evolution.

REFERENCES

Alland, J. J., and C. A. Davis, 2022: Effects of surface fluxes on ventilation pathways and the intensification of Hurricane Michael (2018). *J. Atmos. Sci.*, **79**, 1211–1229, https://doi.org/10.1175/JAS-D-21-0166.1.

——, B. H. Tang, K. L. Corbosiero, and G. H. Bryan, 2021a: Combined effects of midlevel dry air and vertical wind shear on tropical cyclone development. Part I: Downdraft ventilation. *J. Atmos. Sci.*, **78**, 763–782, https://doi.org/10.1175/JAS-D-20-0054.1.

——, ——, ——, and ——, 2021b: Combined effects of midlevel dry air and vertical wind shear on tropical cyclone development. Part II: Radial ventilation. *J. Atmos. Sci.*, **78**, 783–796, https://doi.org/10.1175/JAS-D-20-0055.1.

Alvey, G. R., J. Zawislak, and E. Zipser, 2015: Precipitation properties observed during tropical cyclone intensity change. *Mon. Wea. Rev.*, **143**, 4476–4492, https://doi.org/10.1175/MWR-D-15-0065.1.

——, E. Zipser, and J. Zawislak, 2020: How does Hurricane Edouard (2014) evolve toward symmetry before rapid intensification? A high-resolution ensemble study. *J. Atmos. Sci.*, **77**, 1329–1351, https://doi.org/10.1175/JAS-D-18-0355.1.

——, M. Fischer, P. Reasor, J. Zawislak, and R. Rogers, 2022: Observed processes underlying the favorable vortex repositioning early in the development of Hurricane Dorian (2019). *Mon. Wea. Rev.*, **150**, 193–213, https://doi.org/10.1175/MWR-D-21-0069.1.

Bhatia, K. T., and D. S. Nolan, 2013: Relating the skill of tropical cyclone intensity forecasts to the synoptic environment. *Wea. Forecasting*, **28**, 961–980, https://doi.org/10.1175/WAF-D-12-00110.1.

Boehm, A. M., and M. M. Bell, 2021: Retrieved thermodynamic structure of Hurricane Rita (2005) from airborne multi–Doppler radar data. *J. Atmos. Sci.*, **78**, 1583–1605, https://doi.org/10.1175/JAS-D-20-0195.1.

Cangialosi, J. P., E. Blake, M. DeMaria, A. Penny, A. Latto, E. Rappaport, and V. Tallapragada, 2020: Recent progress in tropical cyclone intensity forecasting at the National Hurricane Center. *Wea. Forecasting*, **35**, 1913–1922, https://doi.org/10.1175/WAF-D-20-0059.1.

Cavallo, S. M., R. D. Torn, C. Snyder, C. Davis, W. Wang, and J. Done, 2013: Evaluation of the advanced hurricane WRF data assimilation system for the 2009 Atlantic hurricane season. *Mon. Wea. Rev.*, **141**, 523–541, https://doi.org/10.1175/MWR-D-12-00139.1.

Chen, S. S., J. A. Knaff, and F. D. Marks Jr., 2006: Effects of vertical wind shear and storm motion on tropical cyclone rainfall asymmetries deduced from TRMM. *Mon. Wea. Rev.*, **134**, 3190–3208, https://doi.org/10.1175/MWR3245.1.

Chen, X., Y. Wang, J. Fang, and M. Xue, 2018a: A numerical study on rapid intensification of Typhoon Vicente (2012) in the South China Sea. Part II: Roles of inner-core processes. *J. Atmos. Sci.*, **75**, 235–255, https://doi.org/10.1175/JAS-D-17-0129.1.

——, M. Xue, and J. Fang, 2018b: Rapid intensification of Typhoon Mujigae (2015) under different sea surface temperatures: Structural changes leading to rapid intensification. *J. Atmos. Sci.*, **75**, 4313–4335, https://doi.org/10.1175/JAS-D-18-0017.1.

——, J. A. Zhang, and F. D. Marks, 2019: A thermodynamic pathway leading to rapid intensification of tropical cyclones in shear. *Geophys. Res. Lett.*, **46**, 9241–9251, https://doi.org/10.1029/2019GL083667.

——, J.-F. Gu, J. A. Zhang, F. D. Marks, R. F. Rogers, and J. J. Cione, 2021: Boundary layer recovery and precipitation symmetrization preceding rapid intensification of tropical cyclones under shear. *J. Atmos. Sci.*, **78**, 1523–1544, https://doi.org/10.1175/JAS-D-20-0252.1.

Corbosiero, K. L., and J. Molinari, 2002: The effects of vertical wind shear on the distribution of convection in tropical cyclones. *Mon. Wea. Rev.*, **130**, 2110–2123, https://doi.org/10.1175/1520-0493(2002)130<2110:TEOVWS>2.0.CO;2.

Cram, T. A., J. Persing, M. T. Montgomery, and S. A. Braun, 2007: A Lagrangian trajectory view on transport and mixing processes between the eye, eyewall, and environment using a high-resolution simulation of Hurricane Bonnie (1998). *J. Atmos. Sci.*, **64**, 1835–1856, https://doi.org/10.1175/JAS3921.1.

Davis, C. A., and Coauthors, 2008a: Prediction of landfalling hurricanes with the Advanced Hurricane WRF Model. *Mon. Wea. Rev.*, **136**, 1990–2005, https://doi.org/10.1175/2007MWR2085.1.

——, S. C. Jones, and M. Riemer, 2008b: Hurricane vortex dynamics during Atlantic extratropical transition. *J. Atmos. Sci.*, **65**, 714–736, https://doi.org/10.1175/2007JAS2488.1.

——, W. Wang, J. Dudhia, and R. Torn, 2010: Does increased horizontal resolution improve hurricane wind forecasts? *Wea. Forecasting*, **25**, 1826–1841, https://doi.org/10.1175/2010WAF2222423.1.

DeHart, J. C., R. A. Houze Jr., and R. F. Rogers, 2014: Quadrant distribution of tropical cyclone inner-core kinematics in relation to environmental shear. *J. Atmos. Sci.*, **71**, 2713–2732, https://doi.org/10.1175/JAS-D-13-0298.1.

DeMaria, M., 1996: The effect of vertical shear on tropical cyclone intensity change. *J. Atmos. Sci.*, **53**, 2076–2088, https://doi.org/10.1175/1520-0469(1996)053<2076:TEOVSO>2.0.CO;2.

——, and J. Kaplan, 1994: A Statistical Hurricane Intensity Prediction Scheme (SHIPS) for the Atlantic basin. *Wea. Forecasting*, **9**, 209–220, https://doi.org/10.1175/1520-0434(1994)009<0209:ASHIPS>2.0.CO;2.

Dunion, J. P., 2011: Rewriting the climatology of the tropical North Atlantic and Caribbean Sea atmosphere. *J. Climate*, **24**, 893–908, https://doi.org/10.1175/2010JCLI3496.1.

Emanuel, K., and F. Zhang, 2017: The role of inner-core moisture in tropical cyclone predictability and practical forecast skill. *J. Atmos. Sci.*, **74**, 2315–2324, https://doi.org/10.1175/JAS-D-17-0008.1.

——, C. DesAutels, C. Holloway, and R. Korty, 2004: Environmental control of tropical cyclone intensity. *J. Atmos. Sci.*, **61**, 843–858, https://doi.org/10.1175/1520-0469(2004)061<0843:ECOTCI>2.0.CO;2.

Finocchio, P. M., and R. Rios-Berrios, 2021: The intensity- and size-dependent response of tropical cyclones to increasing vertical wind shear. *J. Atmos. Sci.*, **78**, 3673–3690, https://doi.org/10.1175/JAS-D-21-0126.1.

Fischer, M. S., B. H. Tang, K. L. Corbosiero, and C. M. Rozoff, 2018: Normalized convective characteristics of tropical cyclone rapid intensification events in the North Atlantic and eastern North Pacific. *Mon. Wea. Rev.*, **146**, 1133–1155, https://doi.org/10.1175/MWR-D-17-0239.1.

——, ——, and ——, 2019: A climatological analysis of tropical cyclone rapid intensification in environments of upper-tropospheric troughs. *Mon. Wea. Rev.*, **147**, 3693–3719, https://doi.org/10.1175/MWR-D-19-0013.1.

——, R. F. Rogers, and P. D. Reasor, 2020: The rapid intensification and eyewall replacement cycles of Hurricane Irma (2017). *Mon. Wea. Rev.*, **148**, 981–1004, https://doi.org/10.1175/MWR-D-19-0185.1.

——, P. D. Reasor, R. F. Rogers, and J. F. Gamache, 2022: An analysis of tropical cyclone vortex and convective characteristics in relation to storm intensity using a novel airborne Doppler radar database. *Mon. Wea. Rev.*, **150**, 2255–2278, https://doi.org/10.1175/MWR-D-21-0223.1.

Frank, W. M., and E. A. Ritchie, 2001: Effects of vertical wind shear on the intensity and structure of numerically simulated hurricanes. *Mon. Wea. Rev.*, **129**, 2249–2269, https://doi.org/10.1175/1520-0493(2001)129<2249:EOVWSO>2.0.CO;2.

Gall, R., J. Franklin, F. Marks, E. N. Rappaport, and F. Toepfer, 2013: The Hurricane Forecast Improvement Project. *Bull. Amer. Meteor. Soc.*, **94**, 329–343, https://doi.org/10.1175/BAMS-D-12-00071.1.

Hardy, S., J. Schwendike, R. K. Smith, C. J. Short, M. J. Reeder, and C. E. Birch, 2021: Fluctuations in inner-core structure during the rapid intensification of Super Typhoon Nepartak (2016). *Mon. Wea. Rev.*, **149**, 221–243, https://doi.org/10.1175/MWR-D-19-0415.1.

Hazelton, A. T., X. Zhang, S. Gopalakrishnan, W. Ramstrom, F. Marks, and J. A. Zhang, 2020: High-resolution ensemble HFV3 forecasts of Hurricane Michael (2018): Rapid intensification in shear. *Mon. Wea. Rev.*, **148**, 2009–2032, https://doi.org/10.1175/MWR-D-19-0275.1.

Hong, S.-Y., J. Dudhia, and S.-H. Chen, 2004: A revised approach to ice microphysical processes for the bulk parameterization of clouds and precipitation. *Mon. Wea. Rev.*, **132**, 103–120, https://doi.org/10.1175/1520-0493(2004)132<0103:ARATIM>2.0.CO;2.

——, Y. Noh, and J. Dudhia, 2006: A new vertical diffusion package with an explicit treatment of entrainment processes. *Mon. Wea. Rev.*, **134**, 2318–2341, https://doi.org/10.1175/MWR3199.1.

Jones, S. C., 1995: The evolution of vortices in vertical shear. I: Initially barotropic vortices. *Quart. J. Roy. Meteor. Soc.*, **121**, 821–851, https://doi.org/10.1002/qj.49712152406.

Judt, F., and S. S. Chen, 2016: Predictability and dynamics of tropical cyclone rapid intensification deduced from high-resolution stochastic ensembles. *Mon. Wea. Rev.*, **144**, 4395–4420, https://doi.org/10.1175/MWR-D-15-0413.1.

Kaplan, J., and Coauthors, 2015: Evaluating environmental impacts on tropical cyclone rapid intensification predictability utilizing statistical models. *Wea. Forecasting*, **30**, 1374–1396, https://doi.org/10.1175/WAF-D-15-0032.1.

Kossin, J. P., and M. D. Eastin, 2001: Two distinct regimes in the kinematic and thermodynamic structure of the hurricane eye and eyewall. *J. Atmos. Sci.*, **58**, 1079–1090, https://doi.org/10.1175/1520-0469(2001)058<1079:TDRITK>2.0.CO;2.

——, and W. H. Schubert, 2001: Mesovortices, polygonal flow patterns, and rapid pressure falls in hurricane-like vortices. *J. Atmos. Sci.*, **58**, 2196–2209, https://doi.org/10.1175/1520-0469(2001)058<2196:MPFPAR>2.0.CO;2.

Kwon, Y. C., and W. M. Frank, 2008: Dynamic instabilities of simulated hurricane-like vortices and their impacts on the core structure of hurricanes. Part II: Moist experiments. *J. Atmos. Sci.*, **65**, 106–122, https://doi.org/10.1175/2007JAS2132.1.

Ladwig, W., 2017: NCAR/wrf-python (version 1.3.0). UCAR/NCAR, accessed 1 June 2022, https://wrf-python.readthedocs.io/en/latest/, https://doi.org/10.5065/D6W094P1.

Leroux, M.-D., M. Plu, D. Barbary, F. Roux, and P. Arbogast, 2013: Dynamical and physical processes leading to tropical cyclone intensification under upper-level trough forcing. *J. Atmos. Sci.*, **70**, 2547–2565, https://doi.org/10.1175/JAS-D-12-0293.1.

Martinez, J., M. M. Bell, J. L. Vigh, and R. F. Rogers, 2017: Examining tropical cyclone structure and intensification with the FLIGHT+ dataset from 1999 to 2012. *Mon. Wea. Rev.*, **145**, 4401–4421, https://doi.org/10.1175/MWR-D-17-0011.1.

Mlawer, E. J., S. J. Taubman, P. D. Brown, M. J. Iacono, and S. A. Clough 1997: Radiative transfer for inhomogeneous atmospheres: RRTM, a validated correlated-k model for the longwave. *J. Geophys. Res.*, **102**, 16 663–16 682, https://doi.org/10.1029/97JD00237.

Montgomery, M. T., and R. K. Smith, 2014: Paradigms for tropical cyclone intensification. *Aust. Meteor. Oceanogr. J.*, **64**, 37–66, https://doi.org/10.22499/2.6401.005.

Munsell, E. B., F. Zhang, J. A. Sippel, S. A. Braun, and Y. Weng, 2017: Dynamics and predictability of the intensification of Hurricane Edouard (2014). *J. Atmos. Sci.*, **74**, 573–595, https://doi.org/10.1175/JAS-D-16-0018.1.

Neelin, J. D., 2007: Moist dynamics of tropical convection zones in monsoons, teleconnections, and global warming. *The Global Circulation of the Atmosphere*, T. Schneider and A. H. Sobel, Eds., Princeton University Press, 267–301.

Nguyen, L. T., and J. Molinari, 2012: Rapid intensification of a sheared, fast-moving hurricane over the Gulf Stream. *Mon. Wea. Rev.*, **140**, 3361–3378, https://doi.org/10.1175/MWR-D-11-00293.1.

——, and ——, 2015: Simulation of the downshear reformation of a tropical cyclone. *J. Atmos. Sci.*, **72**, 4529–4551, https://doi.org/10.1175/JAS-D-15-0036.1.

——, ——, and D. Thomas, 2014: Evaluation of tropical cyclone center identification methods in numerical models. *Mon. Wea. Rev.*, **142**, 4326–4339, https://doi.org/10.1175/MWR-D-14-00044.1.

Nolan, D. S., and L. D. Grasso, 2003: Nonhydrostatic, three-dimensional perturbations to balanced, hurricane-like vortices. Part II: Symmetric response and nonlinear simulations. *J. Atmos. Sci.*, **60**, 2717–2745, https://doi.org/10.1175/1520-0469(2003)060<2717:NTPTBH>2.0.CO;2.

Ooyama, K., 1969: Numerical simulation of the life cycle of tropical cyclones. *J. Atmos. Sci.*, **26**, 3–40, https://doi.org/10.1175/1520-0469(1969)026<0003:NSOTLC>2.0.CO;2.

Rappin, E. D., and D. S. Nolan, 2012: The effect of vertical shear orientation on tropical cyclogenesis. *Quart. J. Roy. Meteor. Soc.*, **138**, 1035–1054, https://doi.org/10.1002/qj.977.

Reasor, P. D., and M. T. Montgomery, 2015: Evaluation of a heuristic model for tropical cyclone resilience. *J. Atmos. Sci.*, **72**, 1765–1782, https://doi.org/10.1175/JAS-D-14-0318.1.

——, ——, and L. D. Grasso, 2004: A new look at the problem of tropical cyclones in vertical shear flow: Vortex resiliency. *J. Atmos. Sci.*, **61**, 3–22, https://doi.org/10.1175/1520-0469(2004)061<0003:ANLATP>2.0.CO;2.

——, R. Rogers, and S. Lorsolo, 2013: Environmental flow impacts on tropical cyclone structure diagnosed from airborne Doppler radar composites. *Mon. Wea. Rev.*, **141**, 2949–2969, https://doi.org/10.1175/MWR-D-12-00334.1.

Riemer, M., and M. T. Montgomery, 2011: Simple kinematic models for the environmental interaction of tropical cyclones in vertical wind shear. *Atmos. Chem. Phys.*, **11**, 9395–9414, https://doi.org/10.5194/acp-11-9395-2011.

——, ——, and M. E. Nicholls, 2010: A new paradigm for intensity modification of tropical cyclones: Thermodynamic impact of vertical wind shear on the inflow layer. *Atmos. Chem. Phys.*, **10**, 3163–3188, https://doi.org/10.5194/acp-10-3163-2010.

——, ——, and ——, 2013: Further examination of the thermodynamic modification of the inflow layer of tropical cyclones by vertical wind shear. *Atmos. Chem. Phys.*, **13**, 327–346, https://doi.org/10.5194/acp-13-327-2013.

Rios-Berrios, R., 2020: Impacts of radiation and cold pools on the intensity and vortex tilt of weak tropical cyclones interacting with vertical wind shear. *J. Atmos. Sci.*, **77**, 669–689, https://doi.org/10.1175/JAS-D-19-0159.1.

——, and R. D. Torn, 2017: Climatological analysis of tropical cyclone intensity changes under moderate vertical wind shear. *Mon. Wea. Rev.*, **145**, 1717–1738, https://doi.org/10.1175/MWR-D-16-0350.1.

——, ——, and C. A. Davis, 2016a: An ensemble approach to investigate tropical cyclone intensification in sheared environments. Part I: Katia (2011). *J. Atmos. Sci.*, **73**, 71–93, https://doi.org/10.1175/JAS-D-15-0052.1.

——, ——, and ——, 2016b: An ensemble approach to investigate tropical cyclone intensification in sheared environments. Part II: Ophelia (2011). *J. Atmos. Sci.*, **73**, 1555–1575, https://doi.org/10.1175/JAS-D-15-0245.1.

——, C. A. Davis, and R. D. Torn, 2018: A hypothesis for the intensification of tropical cyclones under moderate vertical wind shear. *J. Atmos. Sci.*, **75**, 4149–4173, https://doi.org/10.1175/JAS-D-18-0070.1.

Rogers, R. F., P. D. Reasor, and S. Lorsolo, 2013: Airborne Doppler observations of the inner-core structural differences between intensifying and steady-state tropical cyclones. *Mon. Wea. Rev.*, **141**, 2970–2991, https://doi.org/10.1175/MWR-D-12-00357.1.

——, ——, and J. A. Zhang, 2015: Multiscale structure and evolution of Hurricane Earl (2010) during rapid intensification. *Mon. Wea. Rev.*, **143**, 536–562, https://doi.org/10.1175/MWR-D-14-00175.1.

——, ——, J. A. Zawislak, and L. T. Nguyen, 2020: Precipitation processes and vortex alignment during the intensification of a weak tropical cyclone in moderate vertical shear. *Mon. Wea. Rev.*, **148**, 1899–1929, https://doi.org/10.1175/MWR-D-19-0315.1.

Rozoff, C. M., J. P. Kossin, W. H. Schubert, and P. J. Mulero, 2009: Internal control of hurricane intensity variability: The dual nature of potential vorticity mixing. *J. Atmos. Sci.*, **66**, 133–147, https://doi.org/10.1175/2008JAS2717.1.

Ryglicki, D. R., J. D. Doyle, Y. Jin, D. Hodyss, and J. H. Cossuth, 2018: The unexpected rapid intensification of tropical cyclones in moderate vertical wind shear. Part II: Vortex tilt. *Mon. Wea. Rev.*, **146**, 3801–3825, https://doi.org/10.1175/MWR-D-18-0021.1.

——, C. S. Velden, P. D. Reasor, D. Hodyss, and J. D. Doyle, 2021: Observations of atypical rapid intensification characteristics in Hurricane Dorian (2019). *Mon. Wea. Rev.*, **149**, 2131–2150, https://doi.org/10.1175/MWR-D-20-0413.1.

Schecter, D. A., 2008: The spontaneous imbalance of an atmospheric vortex at high Rossby number. *J. Atmos. Sci.*, **65**, 2498–2521, https://doi.org/10.1175/2007JAS2490.1.

——, 2015: Response of a simulated hurricane to misalignment forcing compared to the predictions of a simple theory. *J. Atmos. Sci.*, **72**, 1235–1260, https://doi.org/10.1175/JAS-D-14-0149.1.

——, and M. T. Montgomery, 2003: On the symmetrization rate of an intense geophysical vortex. *Dyn. Atmos. Oceans*, **37**, 55–88, https://doi.org/10.1016/S0377-0265(03)00015-0.

——, and ——, 2007: Waves in a cloudy vortex. *J. Atmos. Sci.*, **64**, 314–337, https://doi.org/10.1175/JAS3849.1.

——, and K. Menelaou, 2020: Development of a misaligned tropical cyclone. *J. Atmos. Sci.*, **77**, 79–111, https://doi.org/10.1175/JAS-D-19-0074.1.

——, M. T. Montgomery, and P. D. Reasor, 2002: A theory for the vertical alignment of a quasigeostrophic vortex. *J. Atmos. Sci.*, **59**, 150–168, https://doi.org/10.1175/1520-0469(2002)059<0150:ATFTVA>2.0.CO;2.

Schubert, W. H., M. T. Montgomery, R. K. Taft, T. A. Guinn, S. R. Fulton, J. P. Kossin, and J. P. Edwards, 1999: Polygonal eyewalls, asymmetric eye contraction, and potential vorticity mixing in hurricanes. *J. Atmos. Sci.*, **56**, 1197–1223, https://doi.org/10.1175/1520-0469(1999)056<1197:PEAECA>2.0.CO;2.

Simpson, R. H., and H. Riehl, 1958: Mid-tropospheric ventilation as a constraint on hurricane development and maintenance. *Tech. Conf. on Hurricanes*, Miami Beach, FL, Amer. Meteor. Soc., D4-1–D4-10.

Smith, R. K., and M. T. Montgomery, 2015: Toward clarity on understanding tropical cyclone intensification. *J. Atmos. Sci.*, **72**, 3020–3031, https://doi.org/10.1175/JAS-D-15-0017.1.

——, and ——, 2016: The efficiency of diabatic heating and tropical cyclone intensification. *Quart. J. Roy. Meteor. Soc.*, **142**, 2081–2086, https://doi.org/10.1002/qj.2804.

——, G. Kilroy, and M. T. Montgomery, 2021: Tropical cyclone life cycle in a three-dimensional numerical simulation. *Quart. J. Roy. Meteor. Soc.*, **147**, 3373–3393, https://doi.org/10.1002/qj.4133.

Sobel, A., S. Wang, and D. Kim, 2014: Moist static energy budget of the MJO during DYNAMO. *J. Atmos. Sci.*, **71**, 4276–4291, https://doi.org/10.1175/JAS-D-14-0052.1.

Stevenson, S. N., K. L. Corbosiero, and J. Molinari, 2014: The convective evolution and rapid intensification of Hurricane Earl (2010). *Mon. Wea. Rev.*, **142**, 4364–4380, https://doi.org/10.1175/MWR-D-14-00078.1.

——, ——, M. DeMaria, and J. L. Vigh, 2018: A 10-year survey of tropical cyclone inner-core lightning bursts and their relationship to intensity change. *Wea. Forecasting*, **33**, 23–36, https://doi.org/10.1175/WAF-D-17-0096.1.

Susca-Lopata, G., J. Zawislak, E. J. Zipser, and R. F. Rogers, 2015: The role of observed environmental conditions and precipitation evolution in the rapid intensification of Hurricane Earl (2010). *Mon. Wea. Rev.*, **143**, 2207–2223, https://doi.org/10.1175/MWR-D-14-00283.1.

Tang, B., and K. Emanuel, 2010: Midlevel ventilation's constraint on tropical cyclone intensity. *J. Atmos. Sci.*, **67**, 1817–1830, https://doi.org/10.1175/2010JAS3318.1.

——, and ——, 2012: Sensitivity of tropical cyclone intensity to ventilation in an axisymmetric model. *J. Atmos. Sci.*, **69**, 2394–2413, https://doi.org/10.1175/JAS-D-11-0232.1.

Tao, D., and F. Zhang, 2014: Effect of environmental shear, sea-surface temperature, and ambient moisture on the formation and predictability of tropical cyclones: An ensemble-mean perspective. *J. Adv. Model. Earth Syst.*, **6**, 384–404, https://doi.org/10.1002/2014MS000314.

——, and ——, 2015: Effects of vertical wind shear on the predictability of tropical cyclones: Practical versus intrinsic limit. *J. Adv. Model. Earth Syst.*, **7**, 1534–1553, https://doi.org/10.1002/2015MS000474.

——, and ——, 2019: Evolution of dynamic and thermodynamic structures before and during rapid intensification of tropical cyclones: Sensitivity to vertical wind shear. *Mon. Wea. Rev.*, **147**, 1171–1191, https://doi.org/10.1175/MWR-D-18-0173.1.

Torn, R. D., 2016: Evaluation of atmosphere and ocean initial condition uncertainty and stochastic exchange coefficients on ensemble tropical cyclone intensity forecasts. *Mon. Wea. Rev.*, **144**, 3487–3506, https://doi.org/10.1175/MWR-D-16-0108.1.

——, and C. A. Davis, 2012: The influence of shallow convection on tropical cyclone track forecasts. *Mon. Wea. Rev.*, **140**, 2188–2197, https://doi.org/10.1175/MWR-D-11-00246.1.

——, and D. Cook, 2013: The role of vortex and environment errors in genesis forecasts of Hurricanes Danielle and Karl

(2010). *Mon. Wea. Rev.*, **141**, 232–251, https://doi.org/10.1175/MWR-D-12-00086.1.

Wadler, J. B., D. S. Nolan, J. A. Zhang, and L. K. Shay, 2021: Thermodynamic characteristics of downdrafts in tropical cyclones as seen in idealized simulations of different intensities. *J. Atmos. Sci.*, **78**, 3503–3524, https://doi.org/10.1175/JAS-D-21-0006.1.

Zhang, C., Y. Wang, and K. Hamilton, 2011: Improved representation of boundary layer clouds over the Southeast Pacific in ARW-WRF using a modified Tiedtke cumulus parameterization scheme. *Mon. Wea. Rev.*, **139**, 3489–3513, https://doi.org/10.1175/MWR-D-10-05091.1.

Zhang, F., and D. Tao, 2013: Effects of vertical wind shear on the predictability of tropical cyclones. *J. Atmos. Sci.*, **70**, 975–983, https://doi.org/10.1175/JAS-D-12-0133.1.

Zhang, G., Z. Wang, T. J. Dunkerton, M. S. Peng, and G. Magnusdottir, 2016: Extratropical impacts on Atlantic tropical cyclone activity. *J. Atmos. Sci.*, **73**, 1401–1418, https://doi.org/10.1175/JAS-D-15-0154.1.